Molecular and Cellular Basis of Spine Morphological Control by Urotensin Signaling

by

Johnathan R. O'Hara-Smith

A dissertation accepted and approved in partial fulfillment of the

requirements for the degree of

Doctor of Philosophy

in Biology

Dissertation Committee:

Kryn Stankunas, Chair

Daniel Grimes, Advisor

Karen Guillemin, Core Member

Judith Eisen, Core Member

Parisa Hosseinzadeh, Institutional Representative

University of Oregon

Summer 2026

© 2026 Johnathan R. O'Hara-Smith

This work is licensed under Creative Commons Attribution 4.0 International. To view a copy of this license, visit https://creativecommons.org/licenses/by/4.0/

DISSERTATION ABSTRACT

Johnathan R. O'Hara-Smith

Doctor of Philosophy in Biology

Title: Molecular and Cellular Basis of Spine Morphological Control by Urotensin Signaling

How animals take shape early, and maintain that shape, is a fundamental question of developmental biology. We investigated this question using zebrafish mutants beginning with studies into how axis straightening, an early and critical process to achieving correct anatomical shape, is controlled. Our insights revealed that two Urotensin II-related peptides, Urp1 and Urp2, initially thought to mediate axis straightening downstream of motile cilia activity, are indeed genetically non-required for this process, but are required to maintain axial shape throughout life. We surprisingly found that loss-of-function mutation of these peptides, or loss of a Urotensin II receptor, Urotensin-2 receptor 3 (Uts2r3), causes complex spinal curvatures beginning around 10 days post fertilization. Intriguingly, we found no hard tissue defects, and no signs of severe muscle breakdown consistent with dystrophy yet observed sweeping transcriptional down-regulation of muscle transcripts in embryos, as well as a highly unique physiological phenotype in muscle. Indeed, measurement of active and passive mechanics using an activator and/or force transducer found that muscle strength is strongly reduced in *uts2r3* mutants, yet tissue stiffness was increased, two physical properties somewhat at odds with each other, since stiffer tissues should be more efficient at translating and transmitting force from activated muscle. The outcomes of these studies inspired further work into how the extracellular matrix (ECM) could explain this unique physiological state, as well as studies on overexpression of *uts2r3*.

This thesis includes previously published co-authored material.

ACKNOWLEDGMENTS

I wish to express sincere gratitude to Professor Daniel Grimes for taking me on as a Research Assistant for over 4 years and funding my doctoral training; and for the moral and intellectual support with all of the work on my manuscript and training along the way. Additionally I want to thank all Grimes lab members, current and former co-workers at all levels, for their contributions to my training and research. I want to sincerely thank all core staff, particularly Judy Peirce and AqACS, Adam Fries at GC3F, and Autumn Wicklund with the media kitchen. Additional thanks to Professors Kryn Stankunas, Karen Guillemin, Judith Eisen, and Parisa Hosseinzadeh for their contributions to the dissertation advisory committee. This work was supported by National Institutes of Health grants R35GM142949, R21HD117423, and R21AG077125.

TABLE OF CONTENTS

Chapter	Page
I. Urotensin Signaling Controls Spine Morphology	7
Introduction	7
Results	8
Discussion	10
Methods	12
II. Chapter 2: Active and Passive Mechanical Deficits Precede Spinal Curvature in a Zebrafish Model of Idiopathic Scoliosis	19
Introduction	19
Results	21
Discussion	31
Methods	33
III. Chapter 3: Transgenic, Bioelectrical, and Histological Studies of Urotensin Mutants	38
Introduction	38
Results	39
Discussion	43
Methods	44
APPENDIX: Supplemental Figures	46
REFERENCES CITED	49

LIST OF FIGURES

Figure Page

1. Urp1 and Urp2 are dispensable for axial straightening. 9

2. *urp1ΔP;urp2ΔP* mutants exhibit adolescent-onset spinal curves without significant structural vertebral defects. 11

3. Loss of *uts2r3* causes spinal curvature and alters muscle-associated gene expression before curve onset. 22

4. *uts2r3* mutants lack overt structural defects but show subtle disruption of muscle organization 24

5. Active force generation is reduced in 5 d.p.f. *uts2r3* mutant larval trunks..... 27

6. Passive mechanical resistance is increased in *uts2r3* mutant axial tissues. 30

7. *smyhc1:gCamp3* illuminates calcium activity in slow muscle. 39

8. Masson's trichrome differentiates fascial, bony, muscular, and other structures in wild type and *uts2r3* and reveals no major differences in morphological features. 41

9. *ubi:uts2r3b1487* develop spinal curvatures during juvenile stages. 42

10. Curves onset gradually in *ubi:uts2r3*^{b1487} 43

11. S1. Muscle organization is grossly normal in *uts2r3* mutants. 46

12. S2. *uts2r3* mutants show subtle muscle disruption at 5 d.p.f. 47

13. S3. Hemisomite area and angle analysis in 14 d.p.f. larvae..... 48

LIST OF TABLES

Table Page

1. Key Resources Table (Chapter 1) – (for Bearce et al., 2023, eLife) 53

2. Key resources table (Chapter 2) – for O'Hara-Smith et al., 2026, bioRxiv 65

Chapter 1: Urotensin Signaling Controls Spine Morphology

Co-authorship acknowledgements: This chapter contains co-authored work published digitally in Bearce et al eLife, January 12, 2023. The mutants used in these studies were created by Dr. Zoe Irons, and phenotypic descriptions, morphometrics, and µct tomography was performed by Dr. Beth Bearce. Samuel Craig, Colin Kuhns, and Sophie Fisher also contributed to the CRISPR screen and embryo imaging. My primary contributions within this co-authored work include the hybridization chain reaction-fluorescent *in situ* hybridization, the quantitative reverse transcriptase Polymerase Chain Reaction work, and the calcein work. Dr. Daniel Grimes wrote the manuscript, made many of the schematics and figures, and conceived the ideas used to generate the manuscript. In addition to this previously published work, Chapter 2 contains work published in my first-author work, O'Hara-Smith et al *bioRxiv*, May 3, 2026. Further breakdown of contributions for O'Hara-Smith et al 2026 can be found in chapter 2.

Introduction

How animals take and maintain shape throughout embryogenesis and then scale that shape through growth is a fundamental question of developmental biology. One of the earliest and most crucial events in body-scale morphogenesis is the process known as axis straightening. Occurring during embryogenesis, axis straightening describes the process by which the embryo unfurls from a curled shape around the yolk and takes on a straight appearance which is maintained generally throughout life.

Critically, early failures in this process in zebrafish were linked to abnormal development of spinal curvature in juvenile stages—specifically, it was shown that control of the activity of motile cilia controlled the coordination of a straight body axis both at the early axis straightening stage and during juvenile spinal shape maintenance (1). When motile cilia are disabled during juvenile development in zebrafish, severe 3-dimensional spinal curvatures resembling idiopathic scoliosis (a human disease characterized by spinal curves due to unknown cause) appear and progress into and throughout adulthood (1). Current work in understanding early shape maintenance focuses heavily on understanding the downstream components between cilia motility and axial straightness and maintenance. A model was developed, based largely on morpholino and

overexpression studies, which suggested the Urotensin 2-related peptides (Urp1 and Urp2) control axis straightening via eliciting slow muscle contraction and somehow aligning the embryo (2, 3). We designed and executed a series of studies to test the hypothesis that signals from motile cilia and its other known immediate downstream mediator of flow signaling (in this context), SCO-spondin (encoded by *sspo)* (3)*,* contributed to both increasing Urotensin signaling via transcriptional upregulation of Urp1 and Urp2 and in turn promoting axis straightening in the embryo.

Results

Our work addressed this model directly by assessing whether these peptides were necessary for axis straightening by creating CRISPR mutants in *urp1* and *urp2* (Fig 1A)*.* Urp1 and Urp2 are small, cyclic, secreted peptides (Fig 1B) expressed beginning roughly around 24-26 hours post fertilization (hpf), coinciding with axial straightening (Fig. 1C). To determine qualitatively whether *urp1* and *urp2* transcripts were diminished, we performed hybridization chain reaction-fluorescent in situ hybridization (HCR-FISH) on *urp1* and *urp2* and found no noticeable reduction in expression (Fig. 1D) at 28 hours post fertilization. Both crispants and mutants for *urp1, urp2, urp1;urp2,* and *uts2r3* failed to phenocopy *cfap298* and *sspo* (Fig. 1E), which was surprising given our hypothesis predicted these to be critical downstream components of the straightening pathway. Although *urp1* and *urp2* were both found to be transcriptionally up-regulated by an upstream motile cilia-derived signal, as *cfap298* and *sspo* mutants were both found to be deficient in *urp1* and *urp2* mRNA transcripts (Fig. 1F). Despite testing in crispants (Fig. 1G) at high numbers, early embryonic body curvatures were not observed among the Urotensin mutants or combination (*urp1;urp2)* mutants (Fig. 1H).

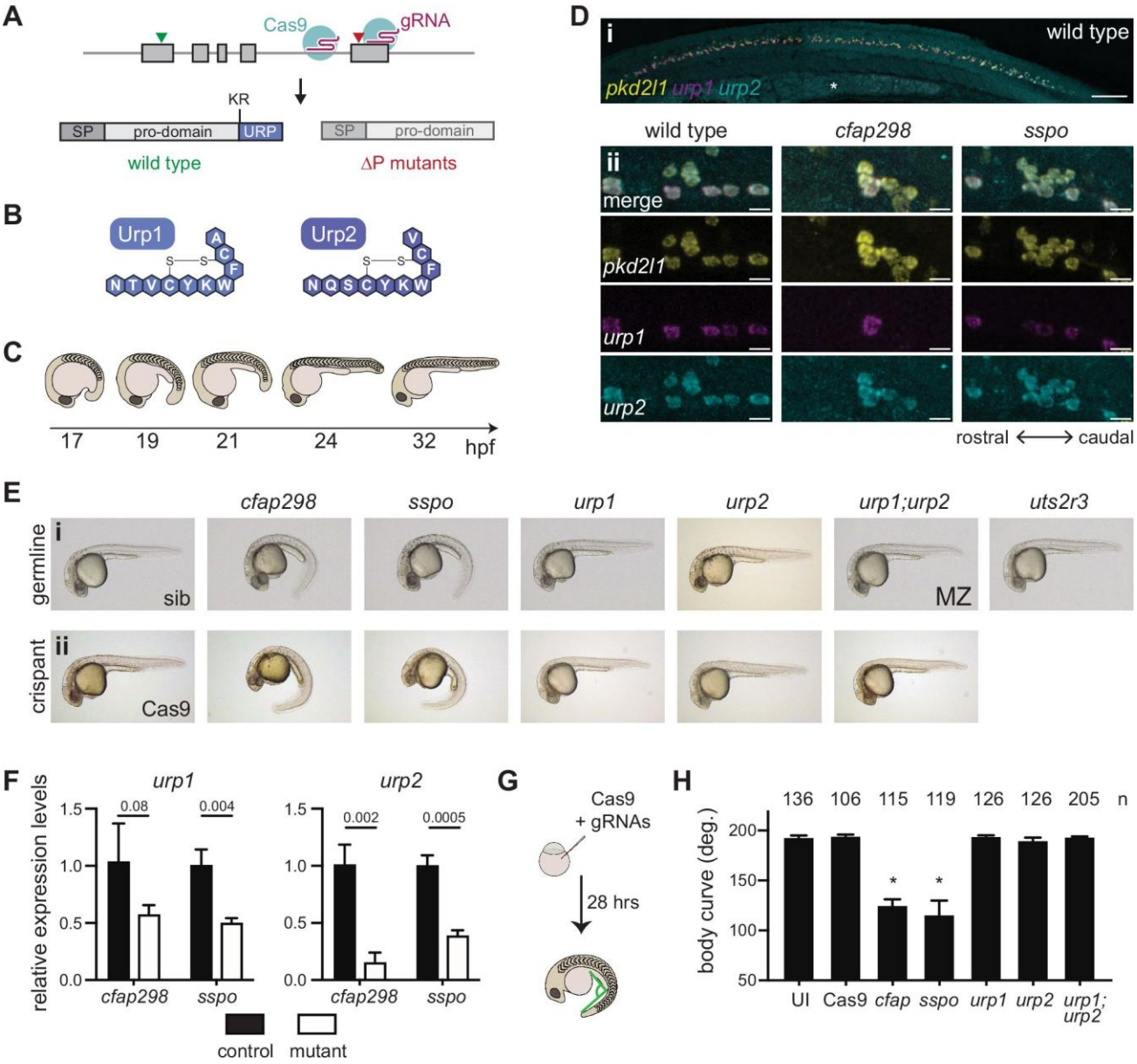


Figure 1. Urp1 and Urp2 are dispensable for axial straightening.

(**A**) *urp1* and *urp2* are 5-exon genes (gray boxes). The final exon codes for the 10-amino acid peptides produced after cleavage from the prodomain at a dibasic site (KR). Pairs of gRNAs were used to induce deletions of Urp1 and Urp2 peptide coding sequences, resulting in $urp1^{\Delta P}$ and $urp2^{\Delta P}$ mutants, respectively. SP – signal peptide. (**B**) Urp1 and Urp2 peptide sequences with identical hexacyclic regions. (**C**) Zebrafish posterior axial straightening, the morphogenetic process which straightens the embryonic body. (**D**) Fluorescence in situ hybridization based on hybridization chain reaction analysis of *pkd2l1*, *urp1,* and *urp2* expression in the central canal at 28 hpf. *pkd2l1* expression marks CSF-cNs. *urp1* expression is restricted to ventral CSF-cNs while *urp2* is expressed in all CSF-cNs. Both *urp1* and *urp2* are expressed in $cfap298^{tm304}$ and $sspo^{b1446}$ mutants, though comparison of

expression between samples was non-quantitative. (**i**) Shows the zebrafish trunk with the yolk stalk labeled (*). (ii) Shows zoomed regions taken at the rostro-caudal level at the end of the yolk stalk. Scale bars: 150 μm (**i**), 10 μm (ii). (**E**) Lateral views of 28–30 hpf germline mutants (**i**) and crispants (ii). The *urp1*$^{\Delta P}$*;urp2*$^{\Delta P}$ double mutants are maternal zygotic (MZ) mutants. Sibling (sib) and Cas9-only injected embryos served as controls. All embryos were incubated at 28°C, which is a restrictive temperature for *cfap298*^{tm304}. (**F**) Quantitative reverse transcriptase PCR (qRT-PCR) analysis of *urp1* and *urp2* mRNA expression levels in *cfap298*^{tm304} and *sspo*^{b1446} mutants at 28 hpf. n>3 biologically independent samples. Bars represent mean ± s.e.m. Two-tailed student's *t* test used to calculate p-values. (**G**) Schematic of crispant generation and body curve analysis. (**H**) Quantitation of crispant body curves where bars represent mean ± s.d. for at least three independent clutches and injection mixes. The total number of embryos analyzed is given. *p<0.0001, student's *t* test applied. UI – uninjected.

Contrary to what would be expected based on morpholino/overexpression studies, *urp1, urp2, urp1;urp2* (combined homozygous knockout), and *uts2r3* (cognate receptor of the peptides) mutation did not yield early embryonic shape defects. However, beginning around 9-11 dpf, *urp1;urp2* and *uts2r3* mutants take on a curved appearance which progresses into a kyphosis/lordosis-like spinal curve phenotype in late juvenile-adult stages (Fig. 2A). These curves are somewhat stereotypical (Fig. 1B-1D) in appearance, especially at younger stages, involving a mostly 2-dimensional (dorsal-ventral) curvature of the spine.

Urotensin mutants have fully penetrant spinal curvatures, and the mechanistic basis of how these curves take shape became a defined question of the field, and generally, the main question of the thesis. To understand whether the vertebral column in Urotensin mutants developed with hard tissue defects, we performed thorough μCT analysis on individual vertebrae and found that there were no hard tissue pattern(s) that explained the basis of spinal curvature (Fig. 2E). Calcein staining of juveniles additionally did not produce any abnormal findings, further indicating no defects in developing vertebrae could be explaining spine morphological breakdown in juvenile *uts2r3* (Fig. 2G).

Discussion

These studies essentially eliminated the model that Urotensin signaling is the downstream mediator between motile cilia-mediated fluid flow and axis straightening.

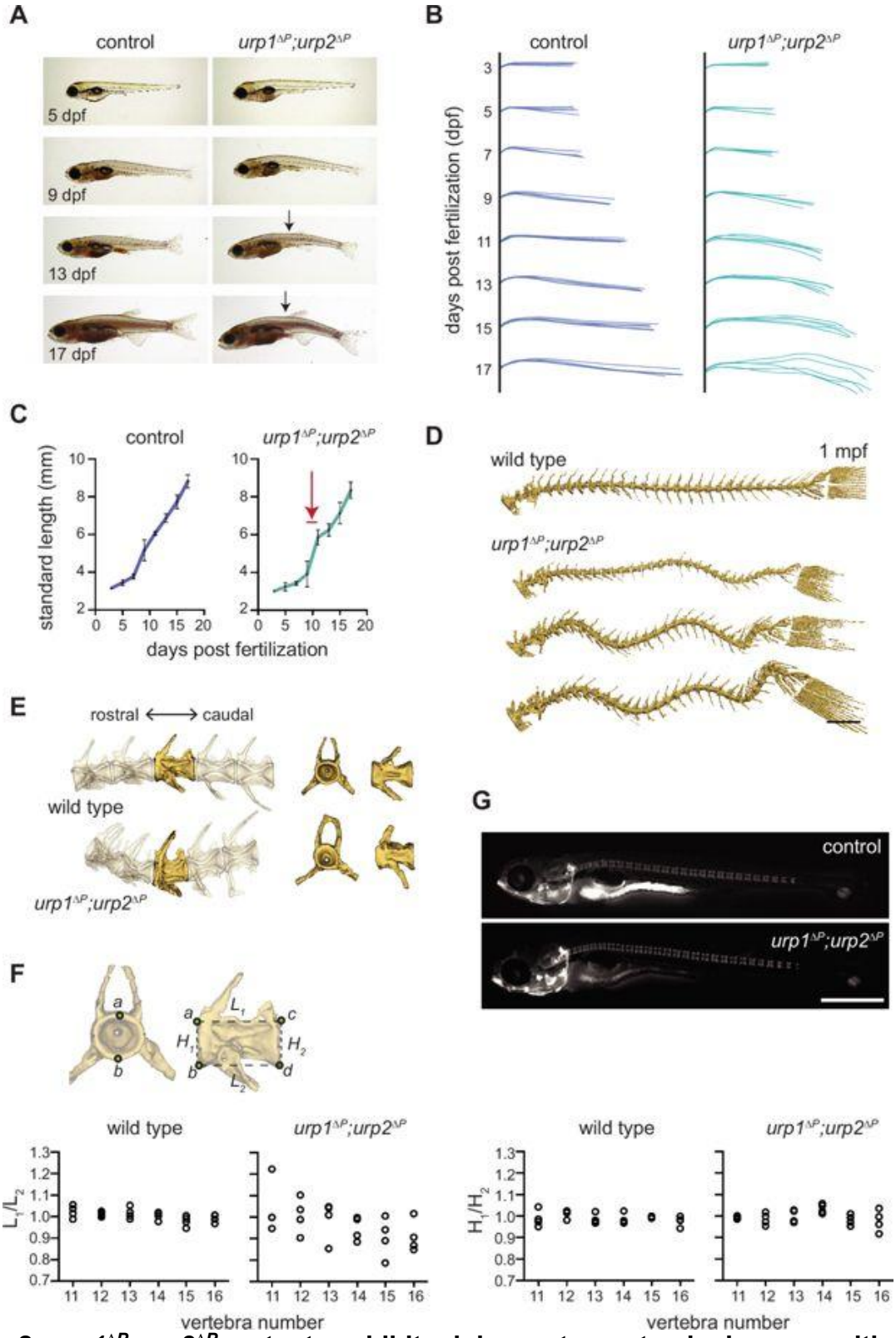


Figure 2. *urp1*$^{\Delta P}$*;urp2*$^{\Delta P}$ mutants exhibit adolescent-onset spinal curves without significant structural vertebral defects.

(**A**) Lateral views of control fish and age-matched *urp1*$^{\Delta P}$;*urp2*$^{\Delta P}$ mutants. Arrows point to forming body curves. (**B**) Traces of body shape every 2 days for 5 fish per time point from 3 to 17 dpf. (**C**) Growth curves for control and *urp1*$^{\Delta P}$;*urp2*$^{\Delta P}$ mutants were indistinguishable. Arrow shows time of curve onset. Mean ± s.d. is plotted. (**D**) Microcomputed tomography (μCT) reconstitutions of spines at 1 mpf with heads, fins, and ribs digitally removed. Scale bar: 1 mm. (**E**) μCT reconstitutions of three pre-caudal and two caudal vertebrae including frontal and lateral views of the highlighted vertebra. No major structural defects such as fusions were observed in *urp1*$^{\Delta P}$;*urp2*$^{\Delta P}$ mutants. (**F**) Vertebral body rostral-caudal length (L_1/L_2) and dorsal-ventral height (H_1/H_2) aspect ratios for six vertebrae of wild type (n=4) and *urp1*$^{\Delta P}$;*urp2*$^{\Delta P}$ mutants (n=4). Length aspect ratios were significantly more variable in mutants, but height aspect ratios were unchanged (p=0.022 and 0.745, respectively, Bartlett's test for equal variances). (**G**) Calcein staining revealed well-structured vertebrae forming in control (standard length 5.7 mm) and *urp1*$^{\Delta P}$;*urp2*$^{\Delta P}$ mutant (standard length 5.7 mm) fish. n>30 fish per condition.

They additionally eliminated one potential pathogenesis mechanism in that no vertebral tissue defects created the opportunity to explore what soft tissue molecular and cellular mechanisms (i.e. breakdown or dysfunction) could contribute to curvatures in Urotensin mutants. Indeed, the focus of our work turned to characterizing how and whether soft tissue defects or differences particularly in muscle tissues, could be related to the cause(s) of spinal curvatures in the model.

Methods

Zebrafish

AB, TU, and WIK strains of D. rerio were used. Zebrafish lines generated were sspob1446, urp1b1420 (called *urp1ΔP*), *urp2*^{b1421} (called *urp2ΔP*), *uts2r3*^{b1436} as well as previously published lines: *cfap298*^{tm304} (4), *pkd2l1*^{icm02} (5), and *sspo-gfp*^{ut24} (6). Experiments were undertaken in accordance with research guidelines of the International Association for Assessment and Accreditation of Laboratory Animal Care and approved by the University of Oregon Institutional Animal Care and Use Committee (Protocol number 21–45). All zebrafish strains and other materials are available upon request.

Generation and genotyping of mutant lines *sspo*^{b1446}, *urp1*^{b1420}, *urp2*^{b1421}, and *uts2r3*^{b1436} were generated using CRISPR/Cas9. gRNA oligos were designed using CRISPRscan (7) gRNA templates (IDT) were assembled by annealing and extension

with Bottom strand ultramer_1 (see key resources table) using Taq Polymerase (NEB, M0273) with cycling parameters of 95°C (3 min), 95°C (30 s), 45°C (30 s), 72°C (30 s), and 72oC (10 min) with 30 cycles of the middle three steps. PCR product was purified (Zymo DNA Clean and Concentrator Kit, D4013) and then used for in vitro RNA synthesis using a MEGAshortscript T7 Transcription Kit (ThermoFisher, AM1354). Synthesized gRNAs were purified (Zymo RNA Clean and Concentrator Kit, R1013), then 150 pg along with 320 pg/nl Cas9 (IDT, 1081058) were injected into one-cell stage fertilized eggs. The mosaic mutant fish resulting from these injections (F0 fish) were raised and outcrossed to AB wild-types, and DNA was extracted from the resulting F1 embryos. Mutant alleles were screened by PCR coupled with restriction enzyme digestion and/or Sanger sequencing (GeneWiz). Embryos from F1 clutches harboring mutations were raised to adulthood and outcrossed to AB wild-types to generate F2 families which were screened for mutations and raised. The nature of mutations was identified by sequencing DNA extracted from adult fin clips of F2 heterozygous fish using CRISP-ID to deconvolute (8) and confirmed by sequencing DNA of F3 homozygous embryos.

urp1^{b1420} mutants contain a 279 bp deletion and 1 bp insertion that were genotyped by PCR amplification with urp1_geno_1 and urp1_geno_2 primers which generate a 460 bp band from wild-type DNA and a 184 bp band from mutant DNA. urp2b1421 mutants harbor a 61 bp deletion and were genotyped by PCR amplification with urp2_geno_1 and urp2_geno_2 primers followed by gel electrophoresis to distinguish the 283 bp wild-type band and the 226 bp mutant band. uts2r3b1436 mutants contain a 534 bp deletion and were also genotyped by PCR, using uts2r3_geno_1 and uts2r3_geno_2, in which wild-type sequence led to an 832 bp band and mutant sequence a 298 bp band.

The nature of the sspob1446 mutation was determined by whole genome sequencing. DNA was extracted from mutant embryos using a phenol/chloroform procedure. Libraries were prepared using the FS DNA Library Prep Kit for Illumina sequencing (NEB, E7805). DNA was digested into 150 bp fragments, and paired-end sequencing was performed using a NovaSeq 6000 Sequencing System. Trimmomatic (version 0.36;

ILLUMNIACLIP: TruSeq3-PE-2.fa:2:30:10:1:true LEADING:3 TRAILING:3 SLIDINGWINDOW:5:20 MINLEN:42 AVGQUAL:30) was used to remove Illumina adaptor sequences from paired-end reads. Illumina short-read sequences were then aligned to the GRCz11 reference sequence of chromosome 24 using BWA-MEM (version 0.7.01). SAMtools (version 1.8) was used to sort and index reads. Aligned reads in BAM format were analyzed in IGV (version 2.13.1). Mutants were routinely genotyped by PCR amplification with oligos sspo_geno_1 and sspo_geno_2, followed by BsaI-HFv2 (NEB, R2733) restriction digestion to produce 300 bp and 99 bp bands from wild-type DNA and a protected 399 bp band from mutant DNA.

Generation of somatic mosaic F0 mutants (crispants)

Four gRNA oligos per gene for cfap298, sspo, urp1, and urp2 were chosen from a look-up table (Key resource appendix; Wu et al., 2018). gRNAs were synthesized from oligos in multiplex. After being pooled at 10 μM, oligos were annealed and extended with Bottom strand ultramer_2 using Phusion High-Fidelity PCR Mastermix (NEB, M0531) with Phusion High-Fidelity DNA Polymerase (NEB, M05030) using incubations: 98 C (2 min), 50 C (10 min), and 72 C (10 min). Assembled oligos were purified and used as template for in vitro RNA synthesis, as described in ‘Generation and genotyping of mutant lines’ section. For mutagenesis, 1000 pg of gRNAs along with 1600 pg/nl Cas9 (IDT, 1081058) were injected into one-cell-stage embryos. To assess rates of mutagenesis, DNA was extracted from 1 dpf crispants and subjected to T7 endonuclease I assays (NEB, E3321).

Quantitation of body curvature at 1–2 dpf

Zebrafish larvae at 28–30 hpf were imaged using a Leica S9i stereomicroscope with integrated 10-megapixel camera. Body angles were calculated using ImageJ (Schindelin et al., 2012) as described in Bearce et al., 2022.

Quantitative reverse transcriptase PCR (qRT-PCR)

RNA was extracted using a Zymo Direct-Zol RNA Miniprep kit (Zymo Research, R2051). cDNA was prepared from 25 ng of RNA using oligoDT primers in a 20 µl reaction using a High Capacity cDNA Reverse Transcription Kit (ThermoFisher, 4368814). qRT-PCR reactions were performed in real time using 5 µl PowerUp SYBR Green Master Mix (ThermoFisher, A25741), 0.8 µl of 10 µM forward and reverse primers, 1.4 µl of nuclease-free water, and 2 µl of diluted cDNA. PCR was performed using a QuantStudio Real Time PCR System (Applied Biosystems) with cycling parameters: 50°C (2 min), 95°C (10 min) then 40 cycles of 95°C (15 s), and 60°C (1 min). Each reaction was performed in quadruplicate. Quantitation was relative to *rpl13* and used the ΔΔCT relative quantitation method in which fold changes are calculated as $2^{-\Delta\Delta CT}$. The efficiency of amplification was verified to be close to 100% with a standard curve of RNA dilutions.

Calcein staining

Larvae were incubated in water containing 0.2% calcein (Sigma-Aldrich, C0875) for 10 min then rinsed two to three times in water (5 min per rinse). Larvae were immobilized with 0.005% tricaine, mounted in 0.8% low melt agarose, and imaged with a Leica THUNDER stereoscope.

Multiplex fluorescent in situ hybridization chain reaction (in situ HCR)

Embryos were fixed in 4% paraformaldehyde at 4°C overnight, washed with phosphate buffered saline (PBS) then serially dehydrated to 100% methanol, and stored at –20°C. Embryos were rehydrated, washed with PBS containing 0.1% Tween-20, incubated in hybridization buffer (Molecular Instruments), then incubated in 2 pmol of probes at 37°C overnight in a total volume of 500 µl of hybridization buffer. Embryos were washed in wash buffer (Molecular Instruments), washed twice in 5× SSCT (sodium chloride sodium citrate with 0.1% tween-20), and then incubated in amplification buffer (Molecular Instruments) for 1 hr. RNA hairpins designed to bind either pkd2l1, urp1, or urp2 were prepared by heating 10 pmol of each to 95°C for 90 s then snap-cooled in the dark for 30 min. Embryos were then incubated overnight in 500 µl of amplification buffer containing 30 pmol hairpins at room temperature in the dark. Embryos were washed five

times in 5× SSCT, stored at 4oC, and then mounted for confocal microscopy. Images were acquired using a Zeiss LSM880 using either a ×20 air or ×40 water objective. Acquisition settings were derived using wild type embryos and then applied to all embryos. Images were exported to IMARIS 9.5.0 (Oxford Instruments). A Gaussian filter of width 0.42 μm (×20) or 0.21 μm (×40), and a rolling ball background subtraction of 10 μm was applied.

X-ray microcomputed tomography

Scans were performed using a vivaCT 80 (Scanco Medical) at 18.5-μm voxel resolution (for 3 mpf and 12 mpf fish) or 10-μm voxel resolution (1 mpf fish) as previously described (9). Digital dissections of the spinal column were performed in 3D Slicer using the Segmentation Editor (10). A threshold of 3200 was used to mask 1 mm tube (Draw Tube function) around the spine in the axial slice view, beginning between the otic vesicles rostral to the first vertebrae and ending at the split of the tail. The center of the tube was set at the narrowest ‘hollow”’ within the lumen of centra.

Quantitation of lateral spine curvature

Quantitation of lateral spine curvature was performed in ImageJ by orienting isolated spine images in a dorsal view with heads to the left and with the otic vesicles and first Weberian vertebrae parallel to the x-axis. Landmarks were assigned to the narrowest point of each centrum rostral to caudal; where maximum projection resulted in hidden or overlapping vertebrae, the appropriate number of points was added in closest approximation. The y-value from each landmark was subtracted from the point rostral to it, resulting in a map of local deflections where positive values indicate rightward displacement, and negative values indicate leftward displacement.

Live imaging of SCOspondin-GFP

Embryos (28 hpf) and larvae (12 dpf) were anesthetized in tricaine until touch response was abolished and then embedded in 0.8% low-melt agarose laced with tricaine in inverted imaging chambers (14 mm #1.5 coverslips, VWR cat no. 10810–054). In larvae, care was taken to align the posterior body close to the coverslip to the RF within

the working distance of the objective. A Nikon Ti2 inverted microscope equipped with Plan Apo ×40 and ×60 WI DIC (1.2 NA) objectives, a Yokogawa Spinning Disk and pco.edge sCMOS camera were used to capture 512×256 images in time series. Exposure time varied with age (100 ms–300 ms) as Sspo-GFP brightened in intensity over time; exposure, camera settings, and laser power were kept constant between age-matched individuals. Images were cropped, rotated, and intensity-adjusted in ImageJ (11).

Bridge

Other preliminary observations into the etiology of spinal curvatures in Urotensin mutants include that they do not have overt difficulties with movement, eating, or mating, indicating that whatever muscular differences or deficiencies exist could be mostly or purely shape-based in nature. Typically, muscular mechanisms of scoliosis are systemic, meaning all tissues with functional skeletal muscle (such as jaw muscle for feeding) undergo cycles of disrepair and imperfect repair, resulting in continuously worsening muscle conditions (chronic dystrophy) (12–14). Identifying these hallmarks (or lack thereof) would be an important part of the thesis work, and, along with physiological description of pre-scioliotic muscle in *uts2r3*, comprise the bulk of the primary literature contribution associated with chapter 2.

Chapter 2: Active and Passive Mechanical Deficits Precede Spinal Curvature in a Zebrafish Model of Idiopathic Scoliosis

Co-authorship acknowledgements: I wanted to acknowledge the mentees, co-workers and advisors who helped make this published work happen. Samuel Bertrand contributed to the analysis and data acquisition for RNA-sequencing work, and Julissa Ortiz-Delatorre assisted with reagent preparation, measurement, and helped facilitate force measurement experiments. Rachael Giersch helped with staining and imaging of the immunofluorescence work. Luke Rethwill assisted with data analysis and performed digital measurements for birefringence work. Dr. Damien Callahan assisted with and performed experiments, conceived ideas for physical measurements, as well as contributed to data analysis and writing of the manuscript. Dr. Daniel Grimes conceived many of the ideas and helped with editing and writing of the manuscript. I wrote the bulk of the manuscript, formed many of the ideas, performed all of the upstream cloning, crossing, and microscopy for the somite quantification work, performed all data acquisition for birefringence, and maintained mutant stock lines for the duration of the work. This work is previously published on *bioRxiv* May 3, 2026.

INTRODUCTION

The emergence and maintenance of body form is a fundamental problem in developmental biology. While early embryonic patterning establishes the basic organization of tissues, preserving correct geometry during growth requires continuous coordination between genetic programs and mechanical environments (15, 16). Failures in this coordination can produce progressive morphological defects with major functional consequences. A prominent example is idiopathic scoliosis (IS), a disorder characterized by rotational lateral spinal curvature that affects approximately 1-4% of populations and most often arises during adolescent growth (17). Despite its prevalence, the biological mechanisms that destabilize axial morphology over time remain poorly understood.

Spinal curvature has long been hypothesized to have a biomechanical origin arising from imbalances in forces acting on the growing spine (18). Classic models propose that axial alignment depends on a balance between active forces generated by

musculature and passive resistance provided by connective tissues, including myofibrillar and tendinous elements and their connection to developing skeletal elements (19–21). Disturbances to this balance are thought to amplify asymmetries in loading and promote progressive curvature during growth (22). Consistent with this view, specific types of scoliosis are associated with neuromuscular or connective tissue disorders (23, 24) such as Duchenne muscular dystrophy (13). Current therapeutic strategies for IS, typically bracing and physiotherapeutic exercise, aim to redistribute mechanical loads (25, 26). However, direct tests of how defined genetic pathways linked to spinal curvature influence the mechanical properties of axial tissues during growth remain limited.

Zebrafish have emerged as a powerful model for investigating the origins of spinal curvature (15, 27). Key features of axial organization are conserved between zebrafish and humans, and many zebrafish mutants develop spinal curves that resemble IS (1, 2, 28–34). Previous work showed that disruption of motile cilia driven cerebrospinal fluid (CSF) flow within the brain ventricles and central canal leads to IS-like spinal curves during larval growth (1). Subsequent studies identified the urotensin II-related peptides, Urp1 and Urp2, as downstream effectors of CSF flow dependent control of body shape (2, 3, 34, 35). These peptides signal through the G protein-coupled receptor Uts2r3, and combined loss of *urp1* and *urp2*, or loss of *uts2r3*, causes juvenile onset spinal curvature in zebrafish (**Fig 1A**; (2, 34, 35)). These findings implicated urotensin signaling in the maintenance of spinal morphology during growth. Uts2r3 is expressed in skeletal muscle during zebrafish development (2), raising the hypothesis that this pathway influences spinal morphology by tuning trunk muscle biomechanics to coordinate the development of skeletal muscle with other rapidly growing tissues in embryonic and juvenile stages.

Here, we tested this hypothesis by combining transcriptomic analysis, imaging of muscle organization, and direct physiological measurements of active and passive mechanical properties in zebrafish *uts2r3* loss of function mutants. By assessing these features before the onset of spinal curvature, we sought to identify early biomechanical defects that could predispose the growing spine to develop the abnormal curvature

typical of *uts2r3* mutants (**Fig. 1A**, (34, 35)). We found that loss of *uts2r3* alters muscle associated gene expression, reduces active force generation elicited from muscle, and increases passive elastic and viscous modulus, despite largely preserved muscle architecture. Together, these results identify urotensin signaling as a pathway that helps maintain spinal morphology by regulating the mechanical state of axial tissues during growth.

RESULTS

Muscle-related gene expression is altered in *uts2r3* mutants

During larval axial morphogenesis, motile cilia-dependent signaling promotes expression of *urp1* and *urp2* in the central canal (2, 34, 35). The Urp1/Urp2 receptor, Uts2r3, is expressed in skeletal muscle (22), suggesting that Urp1/Urp2 might signal directly to muscle tissue. We therefore hypothesized that Urp1/Urp2-Uts2r3 signaling contributes to the maintenance of axial morphology during juvenile growth by modulating muscle development or function (34, 35).

To test this hypothesis, we first performed bulk RNA-sequencing on 28 hours post fertilization (h.p.f.) *uts2r3* loss-of-function mutants and wild-type siblings, using five biological replicates per condition. We then identified genes that were significantly differentially expressed (*padj* < 0.05; **Fig. 1B**). Several muscle-associated genes were downregulated in *uts2r3* mutants, including myosin and skeletal muscle alpha-actin family members (*myo18aa*, *myo18ab*, *acta1a*, *acta1b*), genes associated with myofibrillar structure or myogenesis (*myom1b*, *myot*, *myoz1b*), and genes linked to calcium handling or excitable cell physiology (*casq1a*, *cacn1ha*). Gene ontology enrichment analysis supported this pattern, revealing overrepresentation of muscle-related terms including "skeletal muscle cell," "myofibril assembly," and "skeletal muscle contraction" among differentially expressed genes (**Fig. 1C**). These sequencing results indicate that loss of Uts2r3, a muscle-expressed Urotensin pathway receptor, leads to mis-regulation of muscle-associated genes prior to the onset of spinal curvature.

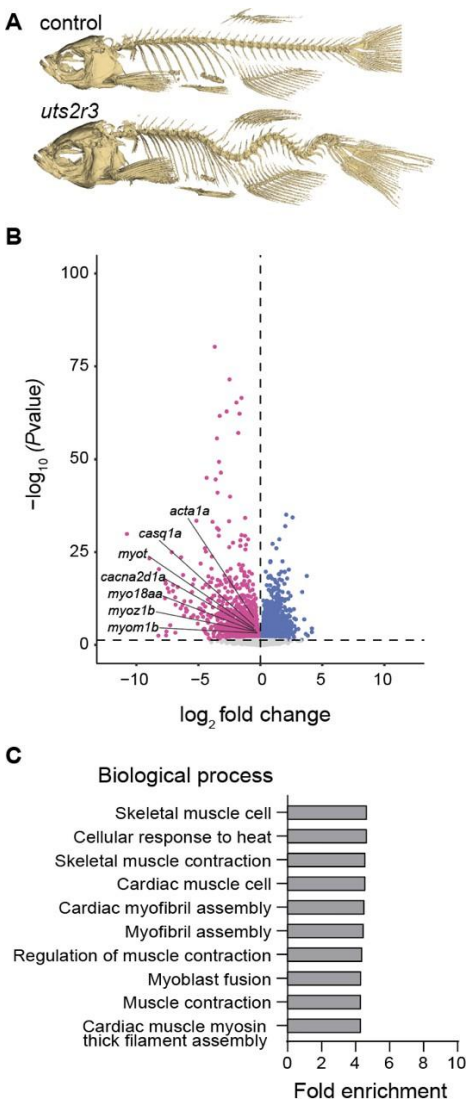


Fig. 1. Loss of uts2r3 causes spinal curvature and alters muscle-associated gene expression before curve onset.

(A) Representative skeletal preparations of adult sibling control and *uts2r3* mutant zebrafish. *uts2r3* mutants develop spinal curvature during juvenile growth. *(B)* Volcano plot of differential gene expression from RNA sequencing of 28 h.p.f. *uts2r3* mutants and wild-type siblings. Highlighted genes are associated with muscle development, myofibrillar organization, contraction, or calcium-dependent physiology. Dashed lines indicate significance and fold change thresholds. *(C)* Gene ontology biological process enrichment analysis of differentially expressed genes, showing enrichment of muscle-associated terms among genes downregulated in *uts2r3* mutants.

uts2r3 mutants lack overt structural defects but show subtle disruption of muscle organization

To assess whether transcriptional changes in *uts2r3* mutants were accompanied by altered muscle architecture, we examined trunk muscle using F-actin labeling and dystrophin immunofluorescence. At 24, 28, and 32 h.p.f., sarcomeric actin organization and dystrophin localization appeared normal in *uts2r3* mutants relative to wild-type siblings, with no obvious disruptions in fiber continuity or segmental patterning (**Fig. 2A** and **Fig. S1**). These results indicate that early transcriptional changes observed in *uts2r3* mutants are not accompanied by gross defects in larval muscle architecture.

We next asked whether more subtle abnormalities emerge later during larval growth by quantifying trunk muscle birefringence. Because birefringence depends on the ordered alignment of myofibrils, reductions in signal provide a sensitive readout of myofibrillar disorganization or misalignment. At 3 and 5 days post fertilization (d.p.f.), *uts2r3* mutants showed a modest but consistent reduction in birefringence intensity compared with wild-type siblings (**Fig. 2B**). However, birefringence patterns remained smooth and continuous, and we did not observe breaks or gaps characteristic of dystrophic muscle mutants ((36, 37)**; Fig. S2**). These data indicate mild disruption of muscle organization without overt dystrophic pathology.

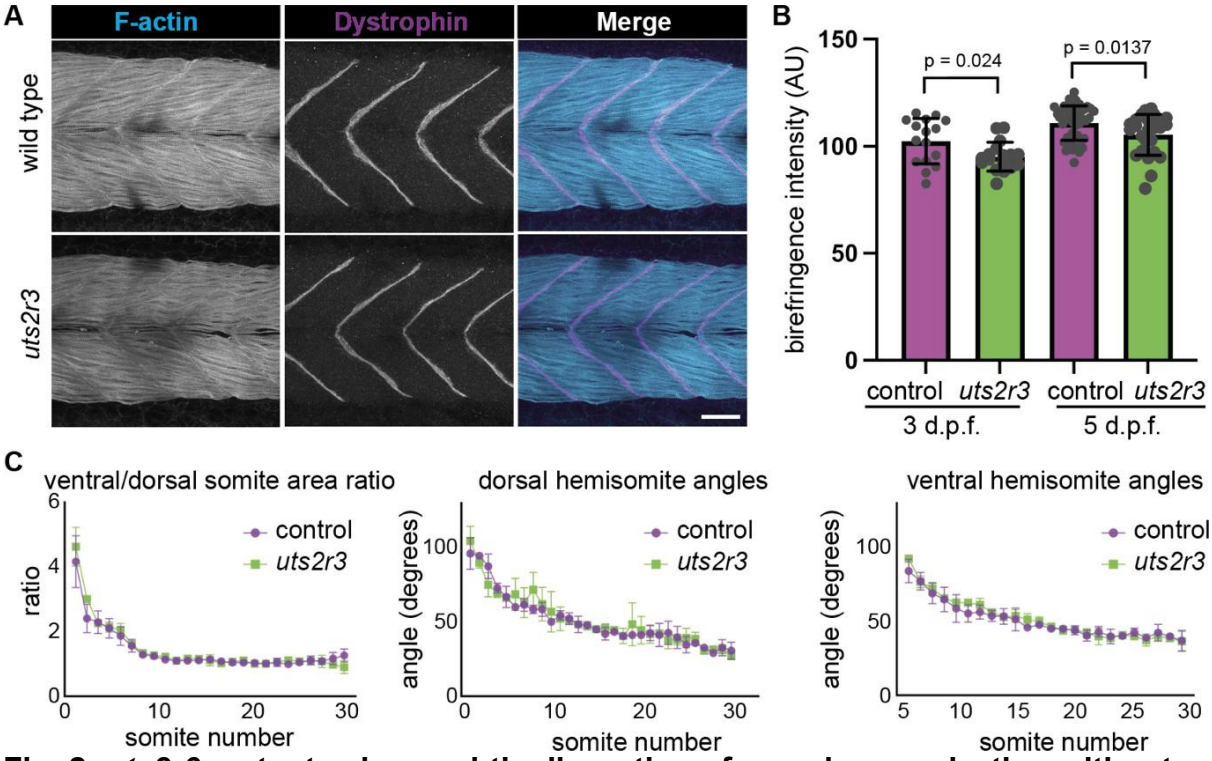


Fig. 2. *uts2r3* mutants show subtle disruption of muscle organization without overt dystrophic pathology or dorsoventral hemisomite asymmetry. *(A)* Representative trunk muscle images from 32 h.p.f. wild-type and *uts2r3* mutant embryos labeled for F-actin and dystrophin. F-actin organization and dystrophin localization appear grossly preserved in *uts2r3* mutants, with no obvious disruption of muscle fiber continuity or myoseptal patterning. Images show equivalent trunk regions acquired at 40x magnification. Scale bar, 20 μm. N ≥ 3 fish examined per condition. *(B)* Quantification of trunk muscle birefringence intensity in 3 d.p.f. and 5 d.p.f. larvae. *uts2r3* mutants showed a modest but significant reduction in mean birefringence intensity at both stages. Data are mean ± SD with individual larvae shown as points. 3 d.p.f.: control, n = 16, *uts2r3*, n = 17. 5 d.p.f.: control, n = 44, *uts2r3*, n = 25. Statistical significance was determined by Student's *t* test. *(C)* Quantification of dorsoventral hemisomite proportions and angles at 14 d.p.f. in sibling-matched control and *uts2r3* mutant larvae carrying the skeletal muscle reporter *Tg(unc503:mVenus-CAAX)*. Ventral-to-dorsal hemisomite area ratios were measured somite-by-somite along the trunk and tail. Dorsal and ventral hemisomite angles were measured relative to the midline. No significant differences were detected between genotypes. Data are mean ± SD. Control, n = 4 larvae; *uts2r3*, n = 3 larvae.

Because asymmetric muscle size and mass have been studied in human contexts as a potential feature underlying or perhaps even driving IS, we next tested whether dorsoventral muscle asymmetry was altered in *uts2r3* mutants (**Fig. S3**). To label myotome morphology, we generated Tg(*unc503:mVenus-CAAX*) transgenic fish in

which the muscle-specific *unc45b* promoter drives mVenus expression in skeletal muscle. Using this line, we measured dorsal and ventral hemisomite area at 14 d.p.f., just as ventrally-directed spinal curves became apparent (24). Despite axial curvature, the ratio of ventral to dorsal hemisomite area in *uts2r3* mutants was indistinguishable from that of sibling controls (**Fig. 2C**). Hemisomite angles relative to the midline were also not unchanged, suggesting that myosepta orientation is preserved in mutants (**Fig. 2C**). These results argue against overt dorsoventral asymmetry in muscle growth as the cause of spinal curvature.

Taken together, these data show that loss of Uts2r3 causes early transcriptional changes and later subtle disruption of muscle organization without gross defects in muscle architecture, dystrophic pathology, or asymmetric muscle growth.

Active muscle force is reduced in *uts2r3* mutants

The subtle structural abnormalities observed in *uts2r3* mutants raised the possibility that urotensin signaling influences inherent muscle function rather than gross muscle architecture or morphology. We therefore asked whether loss of *uts2r3* impairs the ability of axial muscle to generate active force. To test this directly, we measured force production in isolated larval trunk preparations using an apparatus for microscale measurements of force and displacement in contractile tissues that was adapted for use in zebrafish larvae (**Fig. 3A**). Trunk segments were mounted between a force transducer and a length motor using paired sutures (**Fig. 3A**) attaching the specimens to stainless steel hooks, allowing precise measurements of electrically evoked contraction while preserving native tissue organization. Because muscle activation was achieved via an external electrical stimulus, this preparation isolates intrinsic mechanical properties of the muscle while minimizing contributions from motor neurons or locomotor behavior.

Larvae were analyzed at 5 d.p.f., before the onset of spinal curvature but after the emergence of transcriptional changes and reduced muscle birefringence (**Fig. 1B** and **2B**). To determine whether potential differences in force production could be explained by body size or gross morphology, we measured axial dimensions at three standardized positions along the trunk and tail. Axial dimensions did not differ significantly between

uts2r3 mutants and wild-type siblings (p = 0.495; **Fig 3B**). All force measurements (mN) were nevertheless normalized to average specimen cross sectional area to report tension normalized to size ($mN \cdot mm^{-2}$).

Using this preparation, we measured active force generation under two stimulation paradigms. Single twitch contractions, elicited by a brief (400 µs) electrical pulse, report force generated during an individual contraction cycle, whereas tetanic stimulation at high frequency (300 Hz) produces sustained contraction that elicits the maximal force-generating capacity of the muscle. Under both conditions, *uts2r3* mutants generated less force compared with wild-type siblings (**Fig. 3C** and **3D**). This reduction persisted after normalization to axial dimensions (tetanic tension, p = 0.008; **Fig. 3C**), indicating that the deficit reflects reduced intrinsic force-generating capacity rather than differences in specimen size. The reduction was greatest under tetanic conditions, with tetanic tension decreased by approximately 35% in *uts2r3* mutants relative to wild type ($p < 0.05$; **Fig. 3C**).

The reduction in active force observed in *uts2r3* mutants could arise from several distinct mechanisms. Muscle weakness can reflect fewer or weaker force-producing crossbridges (binding events between filamentous actin and the molecular motor, myosin), but it can also result from altered contractile dynamics, such as slowed activation, impaired force transmission across parallel and serial elastic elements (i.e., connective tissue), or exaggerated force loss during shortening. To distinguish between these possibilities, we examined multiple parameters describing the kinetics of muscle contraction using the same intact larval preparation. First, we assessed the relationship between submaximal and maximal force production by quantifying the ratio of twitch force to tetanic force. A twitch contraction elicited by a single 400 µs stimulus reflects force-generating capacity of the tissue and rapid response of its intracellular components to activation and effective transmission of that force through non-contractile tissues. By contrast, tetanic stimulation produces sustained maximal activation and is therefore less reliant on dynamic processes that remain in flux throughout the activation period. Comparing twitch and tetanic force therefore helps reveal whether slowed myosin dynamics or impaired force transmission, which would disproportionately reduce

twitch compared to tetanic force, are playing a role in our outcomes. This ratio did not differ between wild-type (0.87 ± 0.11) and *uts2r3* mutant (0.82 ± 0.13; p = 0.389), indicating preserved scaling between submaximal and maximal activation. Thus, although overall force output is reduced in *uts2r3* mutants, the efficiency with which force is transferred during activation is normal.

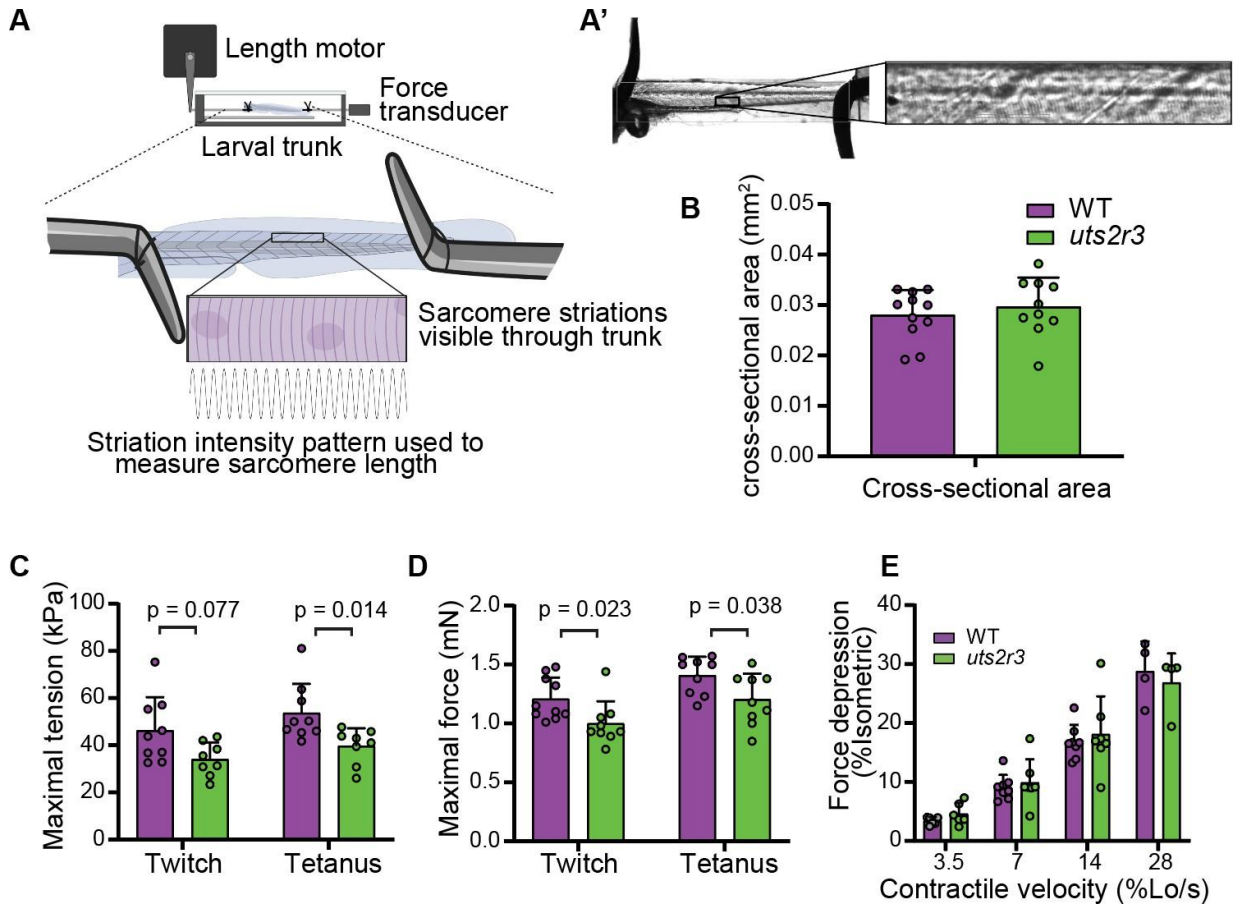


Fig. 3. Active force generation is reduced in 5 d.p.f. *uts2r3* mutant larval trunks.

(A) Schematic of the *ex vivo* larval trunk mechanics assay. Isolated 5 d.p.f. preparations were mounted between a length motor and force transducer for mechanical testing. Sarcomere striations were visualized and used to measure muscle length before mechanical assessment. *(A')* Representative image of a mounted 5 d.p.f. trunk preparation, with the expanded view showing sarcomere striations. *(B)* Cross-sectional area of larval trunk preparations, calculated from dorsal-ventral and lateral diameter

measurements assuming an elliptical cross section. Cross-sectional area did not differ between wild-type and *uts2r3* mutant specimens (p = 0.495; WT, n = 10; *uts2r3*, n = 11). *(C)* Maximal tension generated during twitch and tetanic stimulation. *uts2r3* mutants generated reduced tension compared with wild type, with a significant reduction during tetanic stimulation. WT, n = 9; *uts2r3*, n = 10. *(D)* Maximal force generated during twitch and tetanic stimulation. *uts2r3* mutants generated significantly less force under both stimulation conditions. WT, n = 9; *uts2r3*, n = 10. *(E)* Force depression during shortening contractions, expressed as percent reduction from isometric force at the same length. No significant differences were detected across contractile velocities. WT, n = 8; *uts2r3*, n = 7. Bars show means ± SD with individual specimens shown as points.

Second, the half-relaxation time of twitch contractions, defined as the time required for force to decay from its peak to 50% of peak, was indistinguishable between wild-type (10.3 ± 0.9 ms) and *uts2r3* mutants (10.6 ± 2.4 ms; p = 0.719). This parameter is sensitive to the rates of calcium reuptake and crossbridge detachment and therefore reflects the temporal control of contraction and relaxation. This result therefore indicates normal relaxation kinetics in *uts2r3* mutants.

Finally, because muscle normally shortens while generating force during locomotion, we asked whether *uts2r3* mutant muscle exhibits abnormal force loss during active shortening. In skeletal muscle, force output normally decreases as shortening speed increases, reflecting limits on how rapidly myosin crossbridges can generate force. We quantified this relationship by measuring force-velocity curves during isovelocity contractions across a range of shortening speeds. Across all velocities tested, shortening-dependent force loss was not different between wild type and *uts2r3* mutants (multivariate ANOVA, p > 0.1 for all comparisons; **Fig. 3E**), indicating preserved shortening-dependent modulation of force. Together, these data show that *uts2r3* mutants exhibit a pre-curvature deficit in active force generation despite preserved contractile kinetics.

Passive stiffness of axial tissues is increased in *uts2r3* mutants

Active muscle force represents only one component of the mechanical environment experienced by the developing spine. Forces generated by muscle are transmitted through surrounding tissues, including muscle connective tissue, myosepta, and extracellular matrix, whose passive mechanical properties influence how those forces

are distributed, resisted, and dissipated. In addition, muscle tissue itself has intrinsic viscoelastic properties that contribute to trunk mechanics when it is not actively contracting. We therefore asked whether loss of *uts2r3* alters the passive viscoelastic properties of axial tissues independent of active contraction.

To test this, we measured passive mechanical behavior in intact 5 d.p.f. larval trunks using a stretch-and-hold assay performed in the absence of electrical stimulation on the same force-length apparatus used for active force measurements. By adjusting the lengthener, preparations were subjected to repeated increments of axial strain, each corresponding to 2% of the initial specimen length, followed by a 2 min hold period to allow stress relaxation before the next stretch was applied. This sequence was repeated until specimens reached 156% of their initial length. This approach allowed us to distinguish elastic modulus ("stiffness"), reflected in the stress measured following stress-relaxation, from viscous modulus ("viscosity"), reflected in the time-dependent decay in stress during the hold phase (**Fig. 4A**).

Using this assay, we found that axial tissues from *uts2r3* mutants exhibited increased passive stiffness compared with wild-type siblings. At low strain levels, mechanical behavior was similar between genotypes. At higher strains, however, *uts2r3* mutants displayed significantly elevated passive stress, corresponding to an approximately 35 to 40% increase in modulus at the highest strain tested (multivariate ANOVA at individual strain levels, $p < 0.05$; **Fig. 4A**). This difference was evident both in peak response measured immediately after stretch (**Fig. 4B)** and in stress values measured after relaxation following the hold phase, indicating a robust increase in elastic resistance to deformation in mutant tissues.

Passive viscous behavior, assessed by the time constant of stress relaxation during the hold phase, exhibited greater variability across samples (**Fig. 4C**). Nevertheless, a consistent trend toward increased resistance to prolonged deformation was observed in *uts2r3* mutants (**Fig. 4A-C**). These results show that loss of Uts2r3 increases passive mechanical resistance of axial tissues before spinal curvature begins. Together, our findings show that Uts2r3 helps establish the balance of active and passive mechanical properties that maintain spinal morphology during growth.

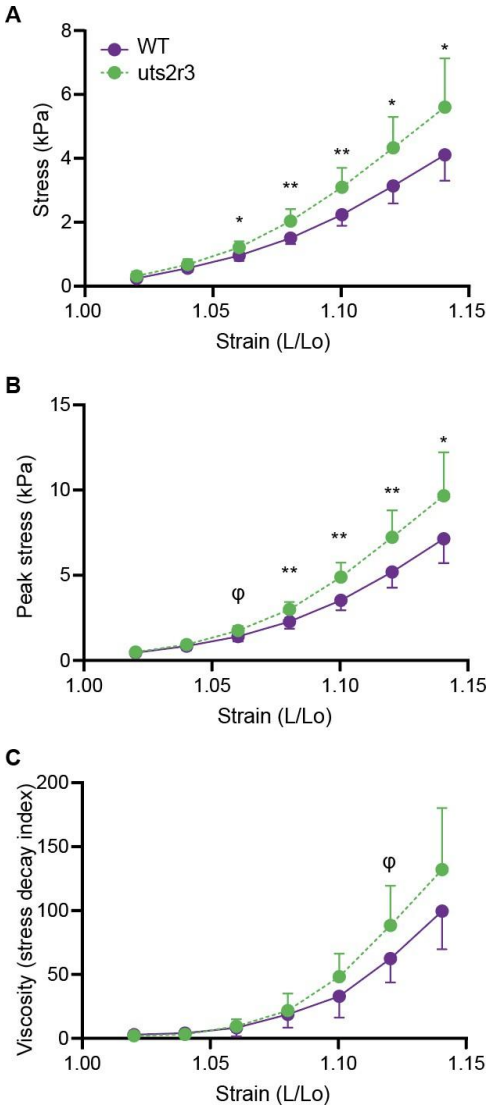


Fig. 4. Passive mechanical resistance is increased in *uts2r3* mutant axial tissues.

(A) Stress-relaxed passive stress measured during stretch-and-hold testing of isolated 5 d.p.f. larval trunk preparations. *uts2r3* mutants showed increased passive stress compared with wild-type siblings, particularly at higher strain levels. *(B)* Peak stress measured immediately after each stretch was also elevated in *uts2r3* mutants. *(C)* Viscous behavior, quantified using the stress decay index during the hold phase, showed a modest trend toward increased viscosity in *uts2r3* mutants. Data show group means ± SD. WT, n = 8; *uts2r3*, n = 5. φ, $p < 0.1$; *, $p < 0.05$; **, $p < 0.01$.

DISCUSSION

Our findings establish *uts2r3* mutants as a model in which altered biomechanics precede and are likely to contribute to IS-like spinal curvature. Before the onset of visible curvature, mutant larvae exhibit a striking combination of reduced active force generation and increased passive resistance to deformation, despite the absence of overt defects in muscle architecture or asymmetric muscle growth. These findings identify a previously unrecognized role for urotensin signaling in regulating the mechanical state of axial tissues during growth.

This mechanical phenotype provides a plausible context for the later emergence of spinal curvature in *uts2r3* mutants. Although it is still unclear whether reduced force generation or increased passive stiffness is sufficient to cause curvature, our data show that both abnormalities are present before curvature begins. We therefore favor a model in which loss of *uts2r3* destabilizes axial mechanics during growth, increasing susceptibility to pathological bending of the body axis. More broadly, these findings support the idea that spinal morphology depends on the continued maintenance of a balanced mechanical environment as the body grows.

uts2r3 mutant axial muscle generates less active force despite largely preserved contractile dynamics. Twitch:tetanus relationships, relaxation kinetics, and force-velocity behavior were all broadly similar between mutants and wild-type siblings, arguing that the reduction in force is not accompanied by gross disruption of contraction timing or shortening-dependent force production. Instead, loss of *uts2r3* appears to reduce overall force-generating capacity while leaving several core physiological properties intact. This interpretation is consistent with our structural data, which show only subtle disruption of muscle organization rather than overt dystrophic pathology.

Loss of *uts2r3* also increases passive mechanical in axial tissues. In the absence of electrical stimulation, mutant trunks resisted stretch more strongly than those of wild-type siblings, especially at higher strain. Because passive mechanics in this preparation likely reflect contributions from muscle together with surrounding connective tissues, myosepta, and extracellular matrix, our data point towards a structural basis of this stiffening phenotype, although the specific tissues or combinations of tissues

responsible remain to be identified. Thus, loss of *uts2r3* alters not only active force production but also the passive viscoelastic properties of the trunk.

Importantly, these active and passive defects are unlikely to be simple consequences of one another. Increased passive stiffness does not readily explain the reduction in active force generation, and the preservation of several contraction kinetics parameters argues against a generalized collapse of muscle function. Instead, *uts2r3* mutants exhibit a distinct mechanical imbalance in which the trunk is both weaker during active contraction and more resistant to passive deformation. Such a state would be expected to alter how forces are generated, transmitted, and absorbed along the growing body axis. We propose that this early imbalance in axial tissue mechanics contributes, directly or indirectly, to the later onset of IS-like curvature in *uts2r3* mutants.

Our results also complement recent work implicating altered tissue mechanics as an early feature of spinal curve pathogenesis in zebrafish. Pumputis et al. showed that oxidative stress induces intervertebral extracellular matrix remodeling, elevated spine stiffness, and later scoliosis-like curvature (38). Importantly, and as for our work, increased stiffness was detectable prior to curve onset (38). Together, these findings support the broader idea that spinal curvature can emerge from early disruption of the mechanical environment of the growing axis across distinct zebrafish models.

A key question raised by this work is how urotensin signaling regulates axial tissue mechanics at the cellular and molecular level. Uts2r3 is expressed in skeletal muscle, but the passive stiffening phenotype could reflect changes in muscle, extracellular matrix, myosepta, or interactions among these tissues. Future work defining the tissue-specific requirements for Uts2r3 and the downstream effectors that alter active and passive mechanics will be important for linking urotensin signaling to the maintenance of axial morphology.

More broadly, our findings argue that spinal curvature cannot be understood from genetic or cellular mechanisms alone. Instead, the effects of developmental pathways must ultimately be interpreted through the tissue-scale mechanical environments they create. Progress in this area will require closer interaction between genetic, cell

biological, and biomechanical approaches, allowing us to understand how molecular changes are transformed into altered forces, stiffness, and progressive changes in body form during growth.

METHODS

Zebrafish

AB strain *D. rerio* were used for all experiments. The transgenic line generated in this study was *Tg*(*unc503:mVenus-CAAX)*^{b1513}. We also used the previously published were *uts2r3*^{b1436} line (24). All experiments were undertaken in accordance with research guidelines of the Association for Assessment and Accreditation of Laboratory Animal Care International and approved by the University of Oregon Institutional Animal Care and Use Committee.

Birefringence quantification and analysis

Zebrafish larvae were placed directly on a polarizing light filter (K&F Concept, B0C2GWS95B) beneath a second polarizing filter (Educational Innovations, TRTV2091) mounted to a custom enclosure. Larvae were positioned with a deer hair (Ted Pella, Inc, 119) to maximize and standardize the birefringence signal. Images were acquired using identical settings on a Leica THUDNER stereoscope. Birefringence was quantified using FIJI (39) by measuring the mean pixel intensity across the contiguous birefringent region of the trunk.

Tg(unc503:mVenus-CAAX) generation

The *Tg(unc503:mVenus-CAAX)* plasmid was generated using Multisite Gateway cloning. Entry clones p5E:*unc503*(Addgene, 64020), pME:*mVenus-CAAX* (Addgene, 75153), and p3E:polyA were combined with the Tol2 destination vector pDest:Tol2-polyA-cryaa:GFP (Addgene, 64022) using LR Clonase II (Ambion, 11791100). The assembly reaction was transformed into NEB 10-beta competent cells.

Individual colonies were selected, plasmid DNA was isolated using the GeneJET Plasmid Miniprep Kit, and the full plasmid was sequenced by Plasmidsaurus to verify the final construct. Transgenesis injections were performed using 25 ng/µL plasmid

DNA and 25 ng/μL Tol2 transposase mRNA. Tol2 mRNA was synthesized using the mMESSAGE mMACHINE kit (Thermo Fisher, AM1344).

Tg(unc503:mVenus-CAAX) imaging

Stable single-copy integrations of Tg(*unc503:mVenus-CAAX*) were generated and used to visualize skeletal muscle morphology. Larvae carrying the transgene were mounted in 1% low-melting-point agarose (Fisher, BP165-25) in petri dishes containing coverslips (Mattek P35G-1.5-10-C). Images were acquired on a Zeiss 880 confocal microscope using a Plan-Apochromat 20x objective. Tiled images were collected with at least 10% overlap between adjacent tiles. Acquisition settings were configured in Zen imaging software using the eYFP channel to detect mVenus-CAAX fluorescence. Image tiles were converted to IMS format using Imaris File Converter 10.2.0 and stitched using Imaris Stitcher 9.9.0 to generate complete trunk images. Stitched images were converted to maximum intensity projections in FIJI. To quantify somite morphology, dorsal and ventral hemisomite boundaries were manually traced as regions of interest, and ROI areas were measured in FIJI. Ventral-to-dorsal hemisomite area ratios were then calculated for each somite. Myoseptal angles were measured from the midline along the visible trajectory of each myoseptum using the angle tool in FIJI.

uts2r3 genotyping by PCR

Genomic DNA was extracted from whole larvae, 14 d.p.f. fin clips, or adult fin tissue by alkaline lysis. Tissue was incubated in 50 mM NaOH (VWR, MK768004) for 20 minutes at 95 C using 50 μL to digest whole larvae or 14 d.p.f. fin clips, and 100 μL for adult fin tissue. Samples were neutralized by adding 5 μL or 10 μL of 1M Tris, pH 7.5 (VWR 97061-794/VWR97061-258) to the 50 μL or 100 μL NaOH lysates,

respectively. PCR genotyping was performed using three primers listed in the Key Resources Table and Taq DNA polymerase with standard buffer (NEB, M0273) for 44 amplification cycles. PCR products were resolved by electrophoresis on 1.5 to 2.0% agarose gels (Topvision Agarose, Thermofisher R0492) with DNA ladder. Genotypes were assigned based on allele-specific banding patterns, using known heterozygous control DNA to confirm successful amplification and band separation.

Bulk RNA-sequencing and differential gene expression analysis.

A DirectZol RNA kit (Zymo Research, R2050) was used to extract total RNA from 28 h.p.f. embryos. A Watchmaker RNA library Prep Kit (Watchmaker Genomics, 7K0078-024) was used for library preparation. Sequencing was performed on an Illumina NextSeq 2000, and trimming was performed using Cutadapt in R (40). Reads were aligned to a zebrafish transcript annotation (41) using the Rsubread package (42) and the resulting alignments were converted to BAM files. Further quality control and short-read quantification was conducted using QuasR (43). Counting of reads and differential gene expression analysis was performed using the DESeq2 package (44). A cutoff of > 0.05 was used for identifying significant hits based on adjusted p-value (*padj*). Gene ontology (GO) enrichment analysis was performed using ShinyGO 0.82 (45), incorporating the “Phenotype.GeneRIF.Predicted” pathway database to identify enriched biological processes among differentially expressed genes.

Phalloidin/MANDRA1/DAPI Staining and Imaging

Embryos from 18-32 h.p.f. were fixed in 4% paraformaldehyde (PFA; Fisher Scientific, 50-980-492), then washed, permeabilized, and blocked. Embryos were incubated with a primary antibody solution containing MANDRA-1 supernatant (DSHB, MANDRA-1S) at a 1:50 dilution, followed by incubation with Hoechst 33258 nuclear stain (1:1000; Sigma-Aldrich, 94403), Phalloidin-AlexaFluor-488 (1:100, Invitrogen/Life Technologies, A12379), and donkey anti-mouse AlexaFluor-647 (1:250; ThermoFisher, A-31571). Embryos were mounted and imaged on a Zeiss LSM 880 confocal microscope.

Active and Passive Mechanical Comparisons

Active contractile function and passive mechanical function were performed as previously described (36). Zebrafish larvae were reared at 28.5 C and maintained at this temperature until immediately before euthanasia. At 5 d.p.f., larvae were anesthetized, decapitated, and the swim bladders were removed using fine forceps (Fine Science Tools, 11255-20). Specimens were immediately transferred to oxygenated Ringer’s solution containing 2.5 mm CaCl2 (Sigma-Aldrich, 21115), 1.2 mM MgCl2 (Sigma-Aldrich, 208337), 1.2 mM KH2PO4 (ThermoFisher, P285), 11.1 mM glucose (TCI,

G0048), 117.2 mM NaCl (Sigma-Aldrich, S9888), 4.7 mM KCl (Sigma-Aldrich, P9333), and 25.2 mM NaHCO3 (ThermoFisher, BP328-500). The solution was equilibrated to pH 7.4 with a mixture of 95% O2 and 5% CO2 and maintained at 18 C for subsequent assays.

Specimens were mounted to a micromanipulator and force transducer, typically used to measure single muscle fiber and muscle tissue composite specimens (Aurora Scientific, Aurora, ON, Canada). This apparatus was customized for these experiments with two stainless steel hooks that were used to mount each specimen at the caudal and rostral ends, secured with four sutures (**Fig. 3A**). Because zebrafish larvae at this stage are semi-translucent at this stage, sarcomere length was measured using an inverted microscope beneath the force-length apparatus. Once secured, specimens were adjusted to a sarcomere length of 1.9 μM, confirmed by observation of thick and thin filament striations.

Active contractile function was measured through field electrical stimulation by assessing the twitch-to-tetanus ratio and force-velocity relationships, as described previously (46). Twitch contractions were elicited using a single 400 μS stimulus, and tetanic contractions were elicited at 300 Hz. Force-velocity relationships were assessed during tetanic stimulation, with tension measured at velocities between 0 and 28 Lo/s. Stimulation was provided using a constant-current stimulation device (Aurora Scientific), with supramaximal current determined independently for each sample preparation before mechanical assessment.

Passive viscoelastic properties, including viscous and elastic modulus, were assessed using stretch-and-hold assays. For these assays, the starting length adjusted to a sarcomere length of = 1.8 μm. Eleven wild type replicates and 11 *uts2r3* mutants were analyzed for the above measures. Outliers from these

assessments, defined as >2 SD from the inclusive group mean, were removed following initial review of aggregate data. In addition, due to technical limitations, some specimens did not provide reliable measures of morphology (n = 1), passive mechanics (n = 3), or active contractile function at velocities of 28 Lo/s (n = 8). Active contractile

force was not assessed under isometric conditions in three *uts2r3* and one wild type specimen.

Passive mechanical assessments were performed after active mechanics in some specimens, but prior activation did not affect material properties in our comparisons. Before passive testing, a single twitch stimulus (400 mA) was delivered to confirm sample integrity. Data are presented as means ± SD unless otherwise noted. Group-level differences between wild type and *uts2r3* larvae were assessed by ANOVA for active contractile properties, including twitch force, tetanic force, twitch tension, tetanic tension, and velocity-specific deficits. Passive viscoelastic properties were assessed using multivariate ANOVA, with significance measured at each degree of strain. Significance was accepted at $p < 0.05$.

Micro-computed tomography (μCT) Imaging

Adult zebrafish were euthanized by hypothermic shock and fixed in 4% PFA for 7 days at 4 C. Fixed specimens were washed twice in 1X PBS to remove residual PFA, then mounted in 0.8% low-melting-point agarose. Specimens were imaged using a ScanCo vivaCT 80 μCT using standard techniques as previously described (20). Three-dimensional reconstructions were generated in 3D Slicer.

Chapter 3: Transgenic, Bioelectrical, and Histological Studies of Urotensin Mutants

Introduction

The physiological state of *uts2r3* reflects a unique combination of muscle traits, and we did not observe signs of muscular dystrophy, this lead to a determination that *uts2r3* and by extension Urotensin mutants indeed have an idiopathic scoliosis-like phenotype. In absence of outright dystrophy, muscle-based curvatures could still be explained by failures in early muscular activity (there is evidence of strength defects at 5 dpf). Further, defects in the myofascial network could potentially explain the unique combination of physiological muscle traits in *uts2r3.* If force cannot be properly transmitted across larger-scale tissues as a result of impaired or imperfect myofascial ECM, the forces that balance gravity to shape the fish's growing spine could partially fail leading to the consistent downward lordosis-like curves in *uts2r3*. Further, since we know there is a muscle weakness deficit in *uts2r3* at 5 dpf, seeing a quantifiable or major difference in a muscle-adjacent tissue could serve as a logical through-line from larval weakness to developmental mis-shaping of the developing spine, as the spine is supported by and can be clearly be influenced by muscular balance/imbalance in disease states. To address this, we directly visualized muscle collagens using Masson's trichrome stain. Masson's trichrome can be used in many biological contexts, and one of its applications is in differentiating extracellular fascia from cellular components of muscle and organs. Since passive stiffness was increased in *uts2r3* and muscle strength was decreased, along with the fact they are not experiencing muscle dystrophy; we hypothesized that myofascial could be weakened, stiffened, or otherwise malformed in *uts2r3*.

We additionally performed transgenic studies, both to assess the effects of overexpression of *uts2r3* and to attempt to build a tissue-specific genetic knockout toolkit to study the roles of genes and their products in development. This is a particularly attractive tool for studying scoliosis-related questions, as it is often difficult to ascertain, in a multi-tissue and multi-organ disease, which tissue or set of tissues are truly causing curvature.

Results

Slow muscle gCamp3 readouts indicate slow muscle calcium activity is largely normal in *uts2r3*

We set out to determine whether early slow muscle calcium transients showed major differences between *uts2r3* and wild type. The rationale for this experiment was that early muscle differences show up in RNA-seq, and larval muscle had notable twitch-excitation deficits. Additionally, previous literature argued Uts2r3 is expressed and functions through embryonic slow muscle.

Wild type and mutant zebrafish displayed highly similar calcium transience patterns when observed at 28-29 hpf, and both sets of samples displayed frequent movements consistent with slow muscle contraction. Although our a priori was mostly directed toward monitoring for excitation and contraction dynamics, it may also be notable we did not notice irregularities in propagation of calcium waves as observed in previous studies on Gjd4 mutants (47). In these studies, there was a similar distribution (defined by the number of flashes or transients defined by 1.5-fold intensity increase over baseline) observed at similar rates for both wild type (n=13) and *uts2r3* (n=9).

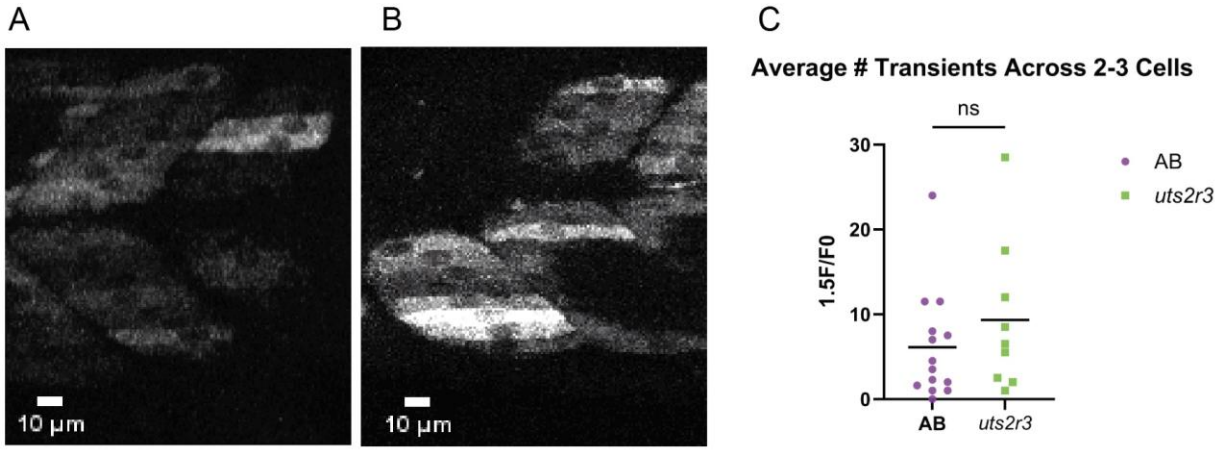


Figure 1: *smyhc1:gCamp3* illuminates calcium activity in slow muscle. A. Still image of wild-type slow muscle with the *smyhc1:gcamp3*^{b1487} line. B. still image of *uts2r3* mutant muscle with the same *smyhc1:gcamp3*. C. 2-3 muscle cells (either adjacent or from the same somite) were measured using the same-size ROI. A baseline of the lowest 10% of the frames captured was set to create a threshold for a calcium transient/activation signal.

Histological examination using Masson's Trichrome staining revealed no major differences in anatomy

To test the hypothesis ECM/muscle fascia could be deficient and contributing to muscle-based scoliosis-like curvatures in *uts23r3,* we used Masson's trichrome to visualize muscle collagen/ECM in zebrafish on the hypothesis that significant changes in ECM deposition patterns at 5 dpf and/or 14 dpf could explain their unique muscle physiological phenotype and contributed to the development of abnormal spine morphology. We found however at 5 dpf (when we reported physiological state differences) and 14 dpf (when the curve state becomes obvious in *uts2r3*) there were no notable differences in muscle appearance, fascia appearance, or vertebral morphology. Specifically, 5 dpf transverse sections showed some staining of intermuscular collagen/ECM in expected locations.

Overexpression of *uts2r3* from the *ubi* promoter caused scoliosis-like curvatures

To determine whether Uts2r3 could have broad or muscle tissue-specific effects, we utilized a transgenic strategy, developing 2 overexpression lines. We created 3+ unique integrations of the *ubi:uts2r3* and 3+ unique integrations of *unc:503:uts2r3*, meaning at least 3 unique founders were identified for each line where multiple founders in any case had at least 50% transmission from f0s. Transmission was identified via GFP expressed from the alpha-crystallin promoter, and was not directly linked to transcription and translation of Uts2r3.

Using eye GFP and inferring via Mendelian ratios among offspring, we identified multiple f1s, and of the derived *ubi* and *unc*-driven Uts2r3 lines (including all generated lines and stages), one line seemed to have phenotypic effects that appeared to be consistent with *uts2r3* overexpression. This line, *ubi:uts2r3*^{b1487} was associated with variable timing-onset scoliosis in juvenile stages (**Fig. 3**) with compromised swimming. The phenotype itself of *ubi:uts2r3* was additionally described as apparent fatigue, as well as consistent upward-bending spine morphology with 3-dimensional curves (*uts2r3* and *urp1;urp2* mutants develop with mostly dorsal-ventral planar curves only). It could be speculated that poorly controlled expression from the *ubi* promoter explains why 3-dimensional curvatures appear in some *ubi:uts2r3*^{b1487} individuals, a feature which seems to only occur in older stage *uts2r3* in apparent later stage spine morphological breakdown. Further, body curves are slower to appear in the overexpression phenotype, only emerging roughly around 16 dpf and at 20% penetrance at that time

point, roughly taking 1.5 months post fertilization to reach full curve penetrance (**Fig. 4**).We did not investigate the landing site, or other variables that might have contributed to only one line of multiple seemingly showing a somewhat Urotensin-like phenotype.

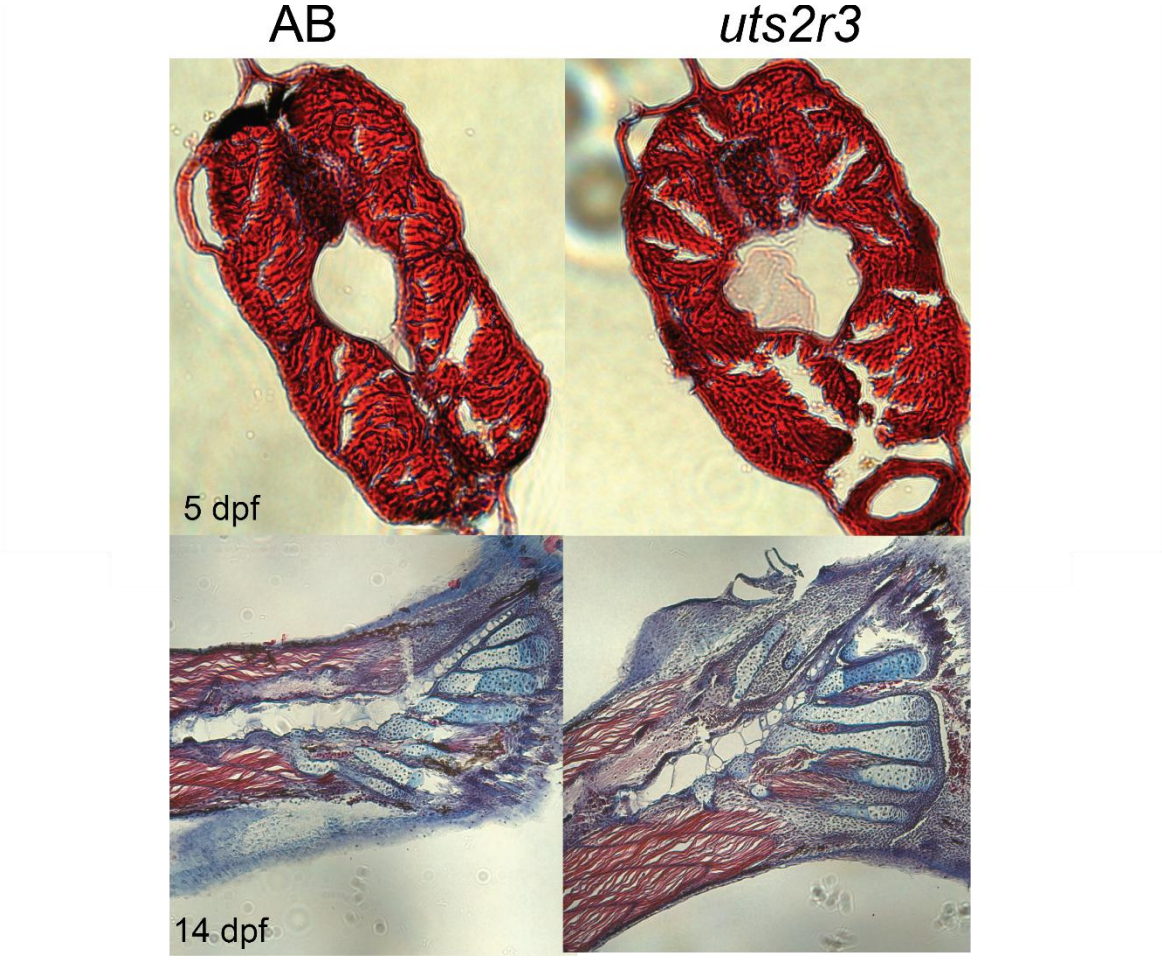


Figure 2: Masson's trichrome differentiates fascial, bony, muscular, and other structures in wild type and *uts2r3* and reveals no major differences in morphological features.

Images were obtained using a Zeiss AxioImager with Axiocam 305. 40x was used for 5 dpf transverse and 10x was used for 14 dpf sagittal sections, representative images.

Tissue-specific knockout lines yielded limited effects

We sought to generate a genetic toolbox of tissue-specific knockout lines for all muscle (*unc503*) (48), slow muscle (*smyhc1*) (49), and notochord (*rcn3*) (16) to build a toolkit for investigating tissue-specific roles for genes in maintaining or developing spine

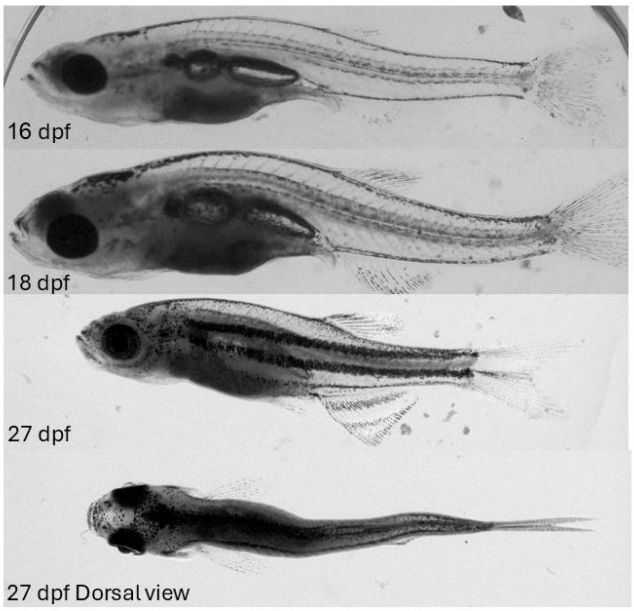


Figure 3: *ubi:uts2r3*^{b1487} develop spinal curvatures during juvenile stages.

Notably, curves bend primarily upward during early stages in the overexpression model, opposite to the downward bends that happen in mutants. Additionally, curves in overexpression frequently were 3-dimensional in nature with obvious lateral deviation.

morphology. We successfully generated Cas9 lines linked with GFP to be expressed in multiple given tissues of interest. However, in all cases tested and observed, f0s showed limited Cas9-GFP expression in target cell types, and progeny never produced an offspring with target tissue expression. This lack of target tissue expression occurred with presumably integrated constructs, as eye GFP expression was frequently observed

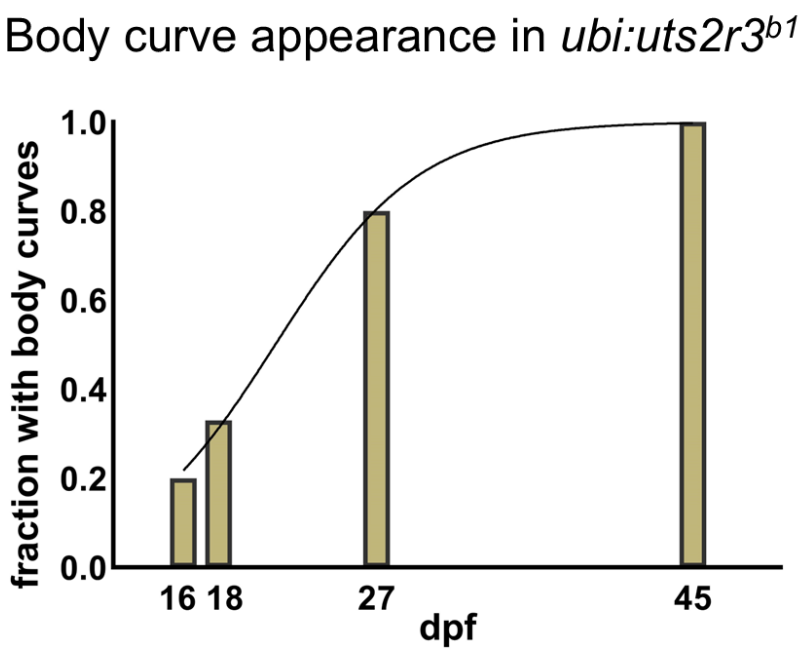


Figure 4: Curves onset gradually in *ubi:uts2r3^{b1487}*.

Unlike *uts2r3* (loss-of-function) mutants, which reach full penetrance in curvature by 16 dpf, at this same time point, *ubi:uts2r3^{b1487}* was 20% penetrant (n=1/5 with curvatures). At 18 dpf, penetrance was 40% (n=3/9), at 27 dpf, 80% (n=8/10) and 100% at 45 dpf (n=19/19).

among injected fish and in some f1s. 5' and 3' UTRs from Xenopus beta-globin were fused to the 5' and 3' terminal ends of the Cas9-GFP mRNA molecule to try to potentially increase expression via stabilization of the mRNA molecule, but this did not increase the abundance of cells expressing GFP within any target tissue type.

Discussion

As far as calcium dynamics determined from gCamp studies, given most contributions to overall physical muscle output measured in physiological studies come from fast muscle, it is somewhat elusive to draw clear parallels between specific outcomes in those physiology studies and this gCamp work. However, it is notable that calcium dynamics (at least at this stage in slow muscle) appear normal; given there are clear muscle contractions observed over this period, it is fair to say that slow muscle calcium propagation, a known upstream mediator of contraction, is normal, and appears to be normally facilitating contractions in slow muscle during embryonic stages.

Histochemical analysis of myofascial with Masson's Trichrome revealed minimal differences in anatomy of muscle fibers and their accompanying fascia/ECM. Lack of positive results in these studies does not necessarily preclude the notion that ECM could be majorly contributing to the shape phenotype in *uts2r3*. Indeed, future directions may seek to look with higher magnification, and/or with alternative stains (e.g. antibodies for specific collagens or other ECM components) to try to find structural differences in muscle that could help explain muscle stiffness and weakness as well as curve phenotype in *uts2r3*.

stages. While this does not necessarily clarify the underlying mechanisms between genetic loss of *uts2r3* and its associated scoliosis-like phenotype, it does rule out a possibility that lost calcium propagation through somites because of mutation could be affecting downstream slow muscle development leading to eventual curvatures.

Methods

gCamp Recording and Measurement

28 hpf uts2r3^{b1436} and wild type (AB) zebrafish with smyhc1:gcamp3^{b1424} were mounted in petri dishes with bottom coverslips (Mattek) in 1.4% low-melting agarose in embryo medium. Imaging was performed with a Leica SP8 confocal microscope with a 40X objective and a 488 nm laser. 7-μm thick Z-stacks were acquired continuously at 700 hz over a period of 330 seconds, equating to roughly 2.13 seconds per stack. Prior to analysis, images were motion-corrected using the reference frames feature in Imaris. Maximum image projections of the motion-corrected images were then generated in ImageJ and a small, equivalently sized ROI was placed in slow muscle cells to measure fluorescence intensity over the recording window. An equivalently sized ROI placed within an in-focus muscle cell was used to avoid biasing of fluorescence means in case cells were partially out of focus, which reduced error. For recording GCamP activity, the bottom 10th percentile of fluorescence intensity means across all frames was used to generate a baseline measurement.

Tissue Processing for Histochemistry

Zebrafish were fixed in 10% neutral buffered formalin and gradually dehydrated in 25/50/75% ethanol (Decon labs)/deionized water before being dehydrated fully into pure

ethanol. Samples were then treated with xylenes to fully remove alcohol, then gradually changed into Paraplast-Xtra (Leica) and full-volume changed at least 3 times to allow full replacement of xylenes with paraffin. Samples were then embedded in Paraplast-Xtra, sectioned at 7 μm, and placed on Superfrost Plus slides (Fisher) with deionized water to adhere tissue to the slide coating.

Masson's Trichrome Staining

Slides were de-waxed with xylenes and rehydrated with ethanol according to StatLab Masson's Trichrome 3000 kit instructions. The mordant step with Bouin's-2000 (StatLab) was performed for 1 hour at 60°C. All downstream staining was performed using kit components and timing of steps was performed according to manufacturer's instructions.

Cloning and Injection of Overexpression and Tissue-Specific Cas9 Constructs

To generate entry vectors to test function of overexpression constructs and tissue-specific knockouts, the gateway cloning system was used. P5e elements (*unc503, ubi, smyhc1, rcn3*), pMe elements (*uts2r3,* Cas9-2A-GFP), P3e elements (*polyA*), and pDest elements (pDest Tol2-pA-crya-GFP) were combined at suggested ratios (10 pmol each for P5e, PMe, P3e, and 20 pmol pDest) and mixed with LR clonase II in TE pH 8 and incubated overnight at room temperature. Transformation of the reaction was then performed into 10 beta cells (NEB) and colonies were picked, screened via full-plasmid sequencing, and injected alongside Tol2 mRNA at 25 ng/μL each.

Appendix

Supplementary Figures

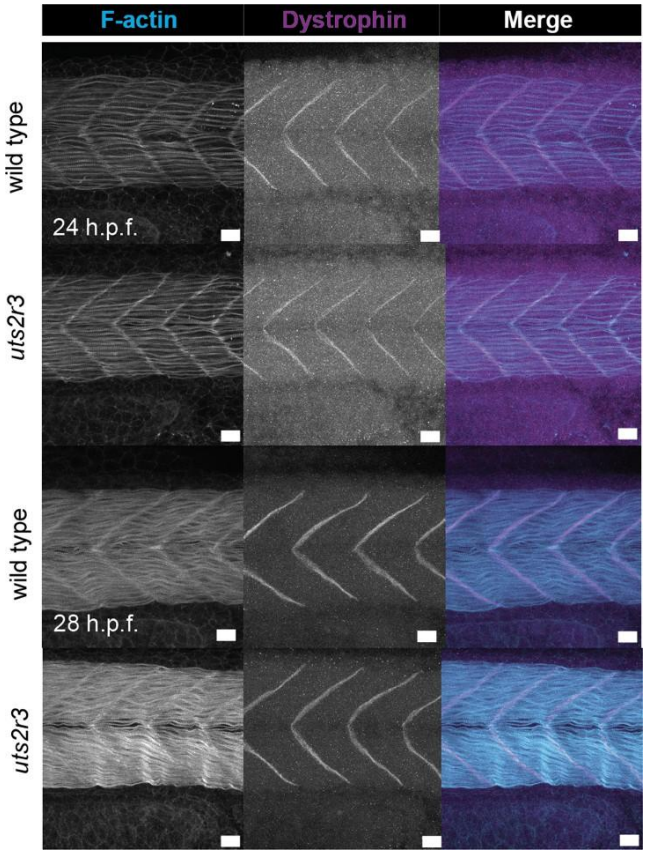


Fig. S1. Muscle organization is grossly normal in *uts2r3* mutants. Representative immunofluorescence images of trunk skeletal muscle in wild-type and *uts2r3* mutant embryos at 24 and 28 h.p.f. F-actin labels filamentous actin and dystrophin labels myosepta. Merged images show overall muscle fiber organization and myoseptal patterning. Images show comparable trunk regions across conditions. Scale bars, 20 μm. N≥3 fish examined per condition.

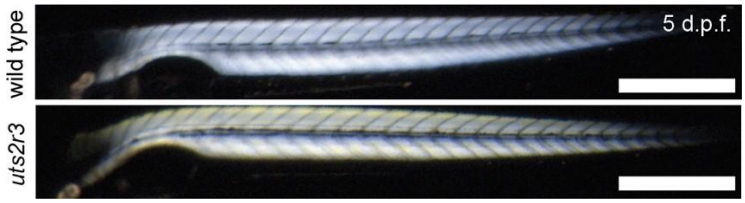


Fig. S2. *uts2r3* mutants show subtle muscle disruption at 5 d.p.f. Representative birefringence images of wild-type and *uts2r3* mutant larvae at 5 d.p.f. *uts2r3* mutants did not display major abnormalities in trunk muscle organization or a pattern consistent with dystrophy-like pathology. Nevertheless, birefringence was modestly but significantly reduced in *uts2r3* mutants compared with wild type. Scale bar, 0.5 mm

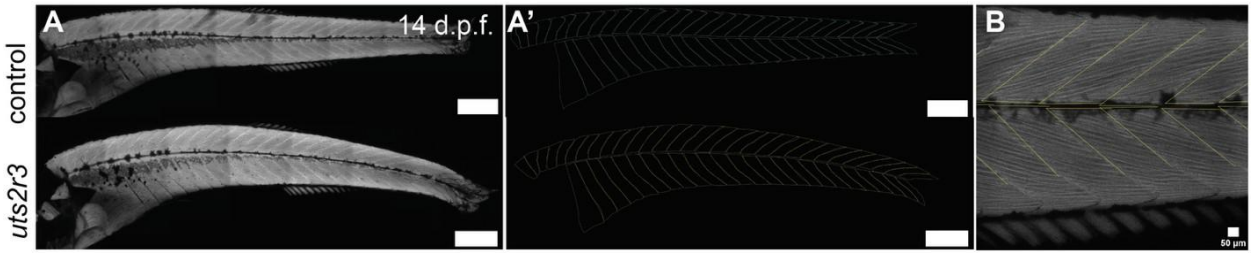


Fig. S3. Hemisomite area and angle analysis in 14 d.p.f. larvae. *(A)* Representative 14 d.p.f. controls and *uts2r3* mutants carrying Tg(*unc503:mVenus-CAAX*). *(A')* Hemisomite abstraction overlay derived from images shown in *A*.

(B) Example of hemisomite angle measurements in a 14 d.p.f. *uts2r3* mutant with typical ventral curvature. Regions of interest were defined in FIJI by tracing angles from the axial midline along adjacent myosepta. Scale bars, 50 µm.

Works Cited

1. D. T. Grimes, *et al.*, Zebrafish models of idiopathic scoliosis link cerebrospinal fluid flow defects to spine curvature. *Science* **352**, 1341–1344 (2016).

2. X. Zhang, *et al.*, Cilia-driven cerebrospinal fluid flow directs expression of urotensin neuropeptides to straighten the vertebrate body axis. *Nat. Genet.* **50**, 1666–1673 (2018).

3. H. Lu, A. Shagirova, J. L. Goggi, H. L. Yeo, S. Roy, Reissner fibre-induced urotensin signalling from cerebrospinal fluid-contacting neurons prevents scoliosis of the vertebrate spine. *Biol. Open* **9**, bio052027 (2020).

4. K. M. Jaffe, *et al.*, c21orf59/kurly controls both cilia motility and polarization. *Cell Rep.* **14**, 1841–1849 (2016).

5. J. R. Sternberg, *et al.*, Pkd2l1 is required for mechanoception in cerebrospinal fluid-contacting neurons and maintenance of spine curvature. *Nat. Commun.* **9**, 3804 (2018).

6. B. R. Troutwine, *et al.*, The Reissner Fiber Is Highly Dynamic In Vivo and Controls Morphogenesis of the Spine. *Curr. Biol.* **30**, 2353-2362.e3 (2020).

7. M. A. Moreno-Mateos, *et al.*, CRISPRscan: designing highly efficient sgRNAs for CRISPR/Cas9 targeting in vivo. *Nat. Methods* **12**, 982–988 (2015).

8. J. Dehairs, A. Talebi, Y. Cherifi, J. V. Swinnen, CRISP-ID: decoding CRISPR mediated indels by Sanger sequencing. *Sci. Rep.* **6**, 28973 (2016).

9. E. A. Bearce, *et al.*, Daw1 regulates the timely onset of cilia motility during development. *Development* **149**, dev200017 (2022).

10. R. Kikinis, S. D. Pieper, K. G. Vosburgh, “3D Slicer: A Platform for Subject-Specific Image Analysis, Visualization, and Clinical Support” in *Intraoperative Imaging and Image-Guided Therapy*, F. A. Jolesz, Ed. (Springer, 2014), pp. 277–289.

11. J. Schindelin, *et al.*, Fiji - an Open Source platform for biological image analysis. *Nat. Methods* **9**, 10.1038/nmeth.2019 (2012).

12. J. Berger, S. Berger, T. E. Hall, G. J. Lieschke, P. D. Currie, Dystrophin-deficient zebrafish feature aspects of the Duchenne muscular dystrophy pathology. *Neuromuscul. Disord.* **20**, 826–832 (2010).

13. J. D. Hsu, R. Quinlivan, Scoliosis in Duchenne muscular dystrophy (DMD). *Neuromuscul. Disord.* **23**, 611–617 (2013).

14. R. Vialle, C. Thévenin-Lemoine, P. Mary, Neuromuscular scoliosis. *Orthop. Traumatol. Surg. Res.* **99**, S124–S139 (2013).

15. M. Bagnat, R. S. Gray, Development of a straight vertebrate body axis. *Dev. Camb. Engl.* **147**, dev175794 (2020).

16. J. Bagwell, *et al.*, Notochord vacuoles absorb compressive bone growth during zebrafish spine formation. *eLife* **9**, e51221 (2020).

17. J. C. Cheng, *et al.*, Adolescent idiopathic scoliosis. *Nat. Rev. Dis. Primer* **1**, 15030 (2015).

18. M. C. Hawes, J. P. O'Brien, The transformation of spinal curvature into spinal deformity: pathological processes and implications for treatment. *Scoliosis* **1**, 3 (2006).

19. M. M. Panjabi, The Stabilizing System of the Spine. Part I. Function, Dysfunction, Adaptation, and Enhancement. *Clin. Spine Surg.* **5**, 383 (1992).

20. A. Bergmark, Stability of the lumbar spine. *Acta Orthop.* 1–54 (1989). https://doi.org/10.3109/17453678909154177.

21. doi:10.1016/S1050-6411(03)00043-9 - 12746520.pdf. Available at: https://www.reprintsdesk.com/userv3/fulltextreader.aspx [Accessed 10 April 2026].

22. I. A. F. Stokes, Analysis and simulation of progressive adolescent scoliosis by biomechanical growth modulation. *Eur. Spine J.* **16**, 1621–1628 (2007).

23. M. Murphy-Ryan, A. Psychogios, N. M. Lindor, Hereditary disorders of connective tissue: A guide to the emerging differential diagnosis. *Genet. Med.* **12**, 344–354 (2010).

24. M. Uehara, J. Takahashi, T. Kosho, Spinal Deformity in Ehlers–Danlos Syndrome: Focus on Musculocontractural Type. *Genes* **14**, 1173 (2023).

25. A. J. Kaelin, Adolescent idiopathic scoliosis: indications for bracing and conservative treatments. *Ann. Transl. Med.* **8**, 28 (2020).

26. H. Kuang, L. Chen, M. Huang, J. Chen, Management of adolescent scoliosis: a comprehensive review of etiology and rehabilitation. *Front. Pediatr.* **13**, 1596400 (2025).

27. C. W. Boswell, B. Ciruna, Understanding Idiopathic Scoliosis: A New Zebrafish School of Thought. *Trends Genet. TIG* **33**, 183–196 (2017).

28. M. Hayes, *et al.*, ptk7 mutant zebrafish models of congenital and idiopathic scoliosis implicate dysregulated Wnt signalling in disease. *Nat. Commun.* **5**, 4777 (2014).

29. J. L. M. Van Gennip, C. W. Boswell, B. Ciruna, Neuroinflammatory signals drive spinal curve formation in zebrafish models of idiopathic scoliosis. *Sci. Adv.* **4**, eaav1781 (2018).

30. C. D. Rose, *et al.*, SCO-Spondin Defects and Neuroinflammation Are Conserved Mechanisms Driving Spinal Deformity across Genetic Models of Idiopathic Scoliosis. *Curr. Biol.* **30**, 2363-2373.e6 (2020).

31. E. A. Terhune, *et al.*, Mutations in KIF7 Implicated in Idiopathic Scoliosis in Humans and Axial Curvatures in Zebrafish. *Hum. Mutat.* 10.1002/humu.24162 (2020). https://doi.org/10.1002/humu.24162.

32. J. G. Buchan, *et al.*, Kinesin Family Member 6 (kif6) Is Necessary for Spine Development in Zebrafish. *Dev. Dyn. Off. Publ. Am. Assoc. Anat.* **243**, 1646–1657 (2014).

33. E. A. Bearce, B. T. B. Ricamona, K. H. Fisher, J. R. O'Hara-Smith, D. T. Grimes, Visualization and quantitation of spine deformity in zebrafish models of scoliosis by micro-computed tomography. *STAR Protoc.* **4**, 102739 (2023).

34. A.-L. Gaillard, *et al.*, Urp1 and Urp2 act redundantly to maintain spine shape in zebrafish larvae. *Dev. Biol.* **496**, 36–51 (2023).

35. E. A. Bearce, *et al.*, Urotensin II-related peptides, Urp1 and Urp2, control zebrafish spine morphology. *eLife* **11**, e83883 (2022).

36. L. L. Smith, A. H. Beggs, V. A. Gupta, Analysis of Skeletal Muscle Defects in Larval Zebrafish by Birefringence and Touch-evoke Escape Response Assays. *J. Vis. Exp. JoVE* 50925 (2013). https://doi.org/10.3791/50925.

37. E. M. Gibbs, E. J. Horstick, J. J. Dowling, Swimming into prominence: the zebrafish as a valuable tool for studying human myopathies and muscular dystrophies. *FEBS J.* **280**, 4187–4197 (2013).

38. P. G. Pumputis, *et al.*, Oxidative stress-induced intervertebral disc remodelling and elevated stiffness drive idiopathic scoliosis in preclinical models. *Nat. Commun.* **16**, 8719 (2025).

39. J. Schindelin, *et al.*, Fiji: an open-source platform for biological-image analysis. *Nat. Methods* **9**, 676–682 (2012).

40. M. Martin, Cutadapt removes adapter sequences from high-throughput sequencing reads. *EMBnet.journal* **17**, 10–12 (2011).

41. N. D. Lawson, *et al.*, An improved zebrafish transcriptome annotation for sensitive and comprehensive detection of cell type-specific genes. *eLife* **9**, e55792.

42. Y. Liao, G. K. Smyth, W. Shi, The R package Rsubread is easier, faster, cheaper and better for alignment and quantification of RNA sequencing reads. *Nucleic Acids Res.* **47**, e47 (2019).

43. D. Gaidatzis, A. Lerch, F. Hahne, M. B. Stadler, QuasR: quantification and annotation of short reads in R.

44. M. I. Love, W. Huber, S. Anders, Moderated estimation of fold change and dispersion for RNA-seq data with DESeq2. *Genome Biol.* **15**, 550 (2014).

45. S. X. Ge, D. Jung, R. Yao, ShinyGO: a graphical gene-set enrichment tool for animals and plants. *Bioinformatics* **36**, 2628–2629 (2020).

46. A. F. Mead, G. G. Kennedy, B. M. Palmer, A. M. Ebert, D. M. Warshaw, Mechanical Characteristics of Ultrafast Zebrafish Larval Swimming Muscles. *Biophys. J.* **119**, 806–820 (2020).

47. R. M. Lukowicz-Bedford, J. S. Eisen, A. C. Miller, Gap-junction-mediated bioelectric signaling required for slow muscle development and function in zebrafish. *Curr. Biol.* **34**, 3116-3132.e5 (2024).

48. J. Berger, P. D. Currie, 503unc, a small and muscle-specific zebrafish promoter. *genesis* **51**, 443–447 (2013).

49. S. Elworthy, M. Hargrave, R. Knight, K. Mebus, P. W. Ingham, Expression of multiple slow myosin heavy chain genes reveals a diversity of zebrafish slow twitch muscle fibres with differing requirements for Hedgehog and Prdm1 activity. *Development* **135**, 2115–2126 (2008).

KEY RESOURCES TABLE (Chapter 1) – (for Bearce et al., 2023, *eLife*)

Reagent type (species) or resource	Designation	Source or reference	Identifiers	Additional information
Commercial assay, kit	DNA Clean and Concentrator Kit	Zymo Research	Cat no: D4013	
Commercial assay, kit	RNA Clean and Concentrator Kit	Zymo Research	Cat no: R1016	
Commercial assay, kit	Direct-zol RNA MiniPrep Kit	Zymo Research	Cat no: R2050	
Commercial assay, kit	GeneJET Gel Extraction Kit	Thermo Fisher Scientific	Cat no: K0691	
Commercial assay, kit	High Capacity RNA-to-cDNA Kit	Thermo Fisher Scientific	Cat no: 4387406	
Commercial assay, kit	MEGAshortscript T7 Transcription Kit	Thermo Fisher Scientific	Cat no: AM1354	
Commercial assay, kit	HiScribe T7 High Yield RNA Synthesis Kit	New England Biolabs	Cat no: E2040	
Commercial assay, kit	FS DNA Library Prep Kit for Illumina	New England Biolabs	Cat no: E7805	
Commercial assay, kit	HCR-RNA FISH	Molecular Instruments		

	Hybridization Buffer			
Commercial assay, kit	T7 Endonuclease I	New England Biolabs	Cat no: E3321	
Commercial assay, kit	HCR-RNA FISH Amplification Buffer	Molecular Instruments		
Commercial assay, kit	AlexaFluor-647 Hairpins	Molecular Instruments		
Commercial assay, kit	AlexaFluor-546 Hairpins	Molecular Instruments		
Commercial assay, kit	AlexaFluor-488 Hairpins	Molecular Instruments		
Commercial assay, kit	urp1 HCR-RNA FISH probe	Molecular Instruments		Project-specific design
Commercial assay, kit	urp2 HCR-RNA FISH probe	Molecular Instruments		Project-specific design
Commercial assay, kit	pkd2l1 HCR-RNA FISH probe	Molecular Instruments		Project-specific design
Commercial assay, kit	Taq Polymerase	New England Biolabs	Cat no: M0273	
Commercial assay, kit	TURBO DNase	Thermo Fisher Scientific	Cat no: AM2238	

Commercial assay, kit	Phusion High-Fidelity DNA Polymerase	New England Biolabs	Cat no: M0530	
Commercial assay, kit	Phusion High-Fidelity PCR Master Mix	New England Biolabs	Cat no: M0531	
Commercial assay, kit	SYBR Green PCR Master Mix	Thermo Fisher Scientific	Cat no: 4309155	
Strain, strain background (Danio rerio)	AB strain	University of Oregon		
Strain, strain background (D. rerio)	WIK strain	University of Oregon		
Strain, strain background (D. rerio)	TU strain	University of Oregon		
Strain, strain background (D. rerio)	*cfap298*^{tm304} line	Jaffe et al., 2016	ZDB-FISH-150901–23024	
Strain, strain background (D. rerio)	*pkd2l1*^{icm02} line	Sternberg et al., 2018	ZDB-FISH-160811–9	
Strain, strain background (D. rerio)	*sspo*^{b1446} line	This study		Figure 1—figure supplement 3

Strain, strain background (D. rerio)	*sspo-GFP^{ut24}* line	Troutwine et al., 2020	ZDB-FISH-190313–20	
Strain, strain background (D. rerio)	*urp1^{b1420}* line	This study		Figure 1—figure supplement 2
Strain, strain background (D. rerio)	*urp2^{b1421}* line	This study		Figure 1—figure supplement 2
Strain, strain background (D. rerio)	*uts2r3^{b1436}* line	This study		Figure 2—figure supplement 3
Software, algorithm	3D Slicer	Fedorov et al., 2012		
Software, algorithm	IMARIS 9.9	Oxford Instruments		
Software, algorithm	NIS-Elements	Nikon Instruments Inc		
Software, algorithm	ZEN Software	Carl Zeiss AG		
Software, algorithm	QuantStudio Design and Analysis Software	Applied Biosystems		
Software, algorithm	Integrated Genome	Robinson et al., 2011		

	Viewer (version 2.13.1)			
Sequence-based reagent	Bottom strand ultramer_1	This study	Tail ultramer for generating singe gRNA oligos	AAAAGCACCGACTCG GTGCCACTTTTTC AAGTTGATAACGG ACT AGCCTTATTTT AACTTGCTAT
Sequence-based reagent	urp1_gRNA_1	This study	gRNA_1 oligo for generating urp1b1 420 line	taatacgactcactataG GCGT TGGTCAGCCTGA CAT gttttagagctagaa
Sequence-based reagent	urp1_gRNA_2	This study	gRNA_2 oligo for generating urp1b1 420 line	taatacgactcactataG GG TCCTCTGTCCATC TCCG gttttagagctagaa
Sequence-based reagent	urp2_gRNA_1	This study	gRNA_1 oligo for generating urp2b1 421 line	taatacgactcactataG GCA GATGGAGAAAGAT TGA gttttagagctagaa
Sequence-based reagent	urp2_gRNA_2	This study	gRNA_2 oligo for generating urp2b1 421 line	taatacgactcactataG GC GTTTGCAGAAATC AGCG gttttagagctagaa
Sequence-based reagent	uts2r3_gRNA	This study	gRNA oligo for generating uts2r3b 1436 line	taatacgactcactataG GG TGAAGGGGAAGA GAAGA gttttagagctagaa
Sequence-based reagent	sspo_gRNA_1	This study	gRNA_1 oligo for generating sspob1 446 line	taatacgactcactataG GT

				CCCCAGTGGTCC GCG GTgttttagagctagaa
Sequenc e-based reagent	sspo_gRNA_2	This study	gRNA_2 oligo for generating sspob1 446 line	taatacgactcactataG GCAC AGTGTGTGAGAC CAG gttttagagctagaa
Sequenc e-based reagent	Bottom strand ultramer_2	This study	Tail ultramer for generating multiplexed gRNA oligos	AAAAGCACCGACT CGG TGCCACTTTTTC AAGTTGATAA CGGACTAGCCTTA TT TTAACTTGCTATTT C TAGCTCTAAAAC
Sequenc e-based reagent	urp1_F0_gRNA_1	Wu et al., 2018	gRNA_1 oligo for generating urp1 F0 embryos	TAATACGACTCAC TAT AGGAAAGTGAAG AT CGCGGCCGTTTTA G AGCTAGAAATAGC
Sequenc e-based reagent	urp1_F0_gRNA_2	Wu et al., 2018	gRNA_2 oligo for generating urp1 F0 embryos	TAATACGACTCAC T ATAGGACACGG CTCTGCC ACAACGTTTTAGA GCTAGAAATAGC
Sequenc e-based reagent	urp1_F0_gRNA_3	Wu et al., 2018	gRNA_3 oligo for generating urp1 F0 embryos	TAATACGACTCAC TA TAGGTTCAGAAGC TGGTAGCAGGTTT TA GAGCTAGAAATAG C

Sequence-based reagent	urp1_F0_gRNA_4	Wu et al., 2018	gRNA_4 oligo for generating urp1 F0 embryos	TAATACGACTCACT ATAGGGAAAATAAAT AACATGGTGTTTTA GAGCTAGAAATAGC
Sequence-based reagent	urp2_F0_gRNA_1	Wu et al., 2018	gRNA_1 oligo for generating urp2 F0 embryos	TAATACGACTCACTA TAGGTGACTGTCGC TTCAATCGGTTTTAG AGCTAGAAATAGC
Sequence-based reagent	urp2_F0_gRNA_2	Wu et al., 2018	gRNA_2 oligo for generating urp2 F0 embryos	TAATACGACTCACT ATAGGGACATTTCCT GACGGAGAGTTTTA GAGCTAGAAATAGC
Sequence-based reagent	urp2_F0_gRNA_3	Wu et al., 2018	gRNA_3 oligo for generating urp2 F0 embryos	TAATACGACTCACTA TAGGTGGACACGA GGAGACCGAGTTTT AGAGCTAGAAATAGC
Sequence-based reagent	urp2_F0_gRNA_4	Wu et al., 2018	gRNA_4 oligo for generating urp2 F0 embryos	TAATACGACTCACT ATAGGTCACCAGGTAG TGACGGAGTTTTAG AGCTAGAAATAGC

Sequence-based reagent	sspo_F0_gRNA_1	Wu et al., 2018	gRNA_1 oligo for generating sspo F0 embryos	TAATACGACTCACT ATAGGTTCGTCCCC AGTGGTCCGGTTTT AGAGCTAGAAATAGC
Sequence-based reagent	sspo_F0_gRNA_2	Wu et al., 2018	gRNA_2 oligo for generating sspo F0 embryos	TAATACGACTCACT ATAGGAAACGG CCGTCAGTGTCG GT TTTAGAGCTAGAA ATAGC
Sequence-based reagent	sspo_F0_gRNA_3	Wu et al., 2018	gRNA_3 oligo for generating sspo F0 embryos	TAATACGACTCAC TATAGGTGTTGC AACACCAACCGG GT TTTAGAGCTAGAA ATAGC
Sequence-based reagent	sspo_F0_gRNA_4	Wu et al., 2018	gRNA_4 oligo for generating sspo F0 embryos	TAATACGACTCACT ATAGGAGCCTAGA CC TGCTCACGGTTTT A GAGCTAGAAATAG C
Sequence-based reagent	cfap298_F0_gRNA_1	Wu et al., 2018	gRNA_1 oligo for generating cfap298 F0 embryos	TAATACGACTCAC TATAGGTTCTCTT CAACACTACGGGT TTTAGAGCTAGAA ATAGC

Sequence-based reagent	cfap298_F0_gRNA_2	Wu et al., 2018	gRNA_2 oligo for generating cfap298 F0 embryos	TAATACGACTCACTATAGGGCTCCACAATCTGATCATGTTTTAGAGCTAGAAATAGC
Sequence-based reagent	cfap298_F0_gRNA_3	Wu et al., 2018	gRNA_3 oligo for generating cfap298 F0 embryos	TAATACGACTCACTATAGGCATTCTTATTGGATCATGGTTTTAGAGCTAGAAATAGC
Sequence-based reagent	cfap298_F0_gRNA_4	Wu et al., 2018	gRNA_4 oligo for generating cfap298 F0 embryos	TAATACGACTCACTATAGGTCTCTGGCAGGTGCGCCCGTTTTAGAGCTAGAAATAGC
Sequence-based reagent	pkd2l1_geno_1	Sternberg et al., 2018	pkd2l1icm02 genotyping oligo 1	TGTGTGCTAGGACTGTGGGG
Sequence-based reagent	pkd2l1_geno_2	Sternberg et al., 2018	pkd2l1icm02 genotyping oligo 2	AGGGCAAGAGAATGGCAAGACG
Sequence-based reagent	urp1_geno_1	This Study	urp1b1420 genotyping oligo 1	GCACCCAAAATCCAACGACT
Sequence-based reagent	urp1_geno_2	This Study	urp1b1420 genotyping oligo 2	TGTATGGGGAAAACAAAGGCA
Sequence-based reagent	urp2_geno_1	This Study	urp2b1421 genotyping oligo 1	TTGGGGTTGTAACAGGTAGTG

Sequence-based reagent	urp2_geno_2	This Study	urp2b1421 genotyping oligo 2	AACAAGGAAGACGCTGCAAG
Sequence-based reagent	uts2r3_geno_1	This Study	uts2r3b1436 genotyping oligo 1	ATGGATCCCCTGATGTCCTG
Sequence-based reagent	uts2r3_geno_2	This Study	uts2r3b1436 genotyping oligo 2	TCGAACTCTGCTCATCCCAG
Sequence-based reagent	sspo_geno_1	This Study	sspob1446 genotyping oligo 1	CGCAAACACTTCCACTTCCA
Sequence-based reagent	sspo_geno_2	This Study	sspob1446 genotyping oligo 2	TTGAAGCCAGATGTAAAGGATGAGTGT
Sequence-based reagent	urp1_gRNA1+2_T7E1_F	This Study	Forward primer to amplify genomic DNA for T7E1 assay in crispants	GACAGCGCACCCTTAATTGT
Sequence-based reagent	urp1_gRNA1+2_T7E1_R	This Study	Reverse primer to amplify genomic DNA for T7E1 assay in crispants	ACATTTAGCCTTAACAAGCACAA
Sequence-based reagent	urp1_gRNA3+4_T7E1_F	This Study	Forward primer to amplify genomic DNA for T7E1 assay in crispants	CAGACAAGGGAACAGAGAGGA
Sequence-based reagent	urp1_gRNA3+4_T7E1_R	This Study	Reverse primer to amplify genomic DNA for T7E1 assay in crispants	CCACTGCTTTTAAATCATCCACC
Sequence-based reagent	urp2_gRNA1_T7E1_F	This Study	Forward primer to amplify genomic DNA for T7E1 assay in crispants	ATCTTAGAGGCGCATTGGTG

Sequence-based reagent	urp2_gRNA1_T7E1_R	This Study	Reverse primer to amplify genomic DNA for T7E1 assay in crispants	GCATGAGGCG GTTTGTTTTG
Sequence-based reagent	urp2_gRNA2+3_T7E1_F	This Study	Forward primer to amplify genomic DNA for T7E1 assay in crispants	TGAAGCAACT GAGGAGCAAA
Sequence-based reagent	urp2_gRNA2+3_T7E1_R	This Study	Reverse primer to amplify genomic DNA for T7E1 assay in crispants	ACAGTACAGTT CAGCACACCT
Sequence-based reagent	urp2_gRNA4_T7E1_F	This Study	Forward primer to amplify genomic DNA for T7E1 assay in crispants	TGACCTATACATC AAAGCCAAGG
Sequence-based reagent	urp2_gRNA4_T7E1_R	This Study	Reverse primer to amplify genomic DNA for T7E1 assay in crispants	CCTGGGCTGA TCATACCTCT
Sequence-based reagent	rpl13_qPCR_F	This Study	Forward primer for quantitative RT-PCR	TAAGGACGGAG TGAACAACCA
Sequence-based reagent	rpl13_qPCR_R	This Study	Reverse primer for quantitative RT-PCR	CTTACGTCTGC GGATCTTTCTG
Sequence-based reagent	urp1_qPCR_F	This Study	Forward primer for quantitative RT-PCR	ACATTCTGG CTGTGGTTTG
Sequence-based reagent	urp1_qPCR_R	This Study	Reverse primer for quantitative RT-PCR	GTCCGTCTTCA ACCTCTGCTAC
Sequence-based reagent	urp2_qPCR_F	This Study	Forward primer for quantitative RT-PCR	AGAGGAAACA GCAATGGACG

Sequence-based reagent	urp2_qPCR_R	This Study	Reverse primer for quantitative RT-PCR	TGTTGGTTTTGGTTGACG

Key resources table (Chapter 2) – for O'Hara-Smith et al., 2026, *bioRxiv*

Reagent, Equipment, or Software Name	Type	Source/Supplier	Identifiers/Additional Information
Polarizing Light Filter	Equipment	Amazon (K&F Concept)	B0C2GWS95B
Polarizing Light Filter Paper	Equipment	Amazon (Educational Innovations)	TRTV2091
Deer Hair Micromanipulator	Equipment	Ted Pella, Inc	119
Low-melting agarose	Reagent	Fisher	BP165-25
Glass-bottom (cover slip) petri dish	Equipment	Mattek	P35G-1.5-10-C
Sodium Hydroxide	Reagent	VWR	MK768004
Tris Base	Reagent	VWR	97061-794
Tris HCl	Reagent	VWR	97061-258
uts2r3_seq_f1	Primer	IDT	TCTCTTGTTTCCCCTCTTTTACC
uts2r3_seq_r1	Primer	IDT	TCTCCCCAAAGCTGCATACA
uts2r3_seq_thirdprimer	Primer	IDT	AAGGAGAAGTACTAGGGT
Taq Dna Polymerase with Standard *Taq* buffer	Reagent	NEB	M0273

Topvision Agarose	Reagent	Thermofisher Scientific	R0492
Imaris File Converter 10.2.0	Software	Imaris	Version 10.2.0
Imaris Stitcher 9.9.0	Software	Imaris	Version 9.9.0
DirectZol RNA Kit	Reagent	Zymo	R2050
Nuclease-free water	Reagent	New England Biolabs	B1500
PolyA Selection Module	Reagent	New England Biolabs	E3370
Watchmaker RNA library Prep Kit	Reagent	Watchmaker Genomics	7K0078-024
KAPA Library Quantification Kit	Reagent	Roche Sequencing	KK4835
Quantsudio 5	Equipment	Life Technologies	
NextSeq 2000	Equipment	Illumina	
NaCl	Reagent	VWR	JT3624-7
Na2HPO4	Reagent	Fisher	02-004-224
NaH2PO4	Reagent	VWR	JT3818-5
Triton X-100	Reagent	Sigma	T8787
NSS	Reagent	Jackson Immunoresearch	013-000-121

dimethyl-sulfoxide	Reagent	Sigma-Aldritch	D8418
Tween-20	Reagent	Sigma	P9416
MANDRA-1 supernatant	Reagent	Developmental Studies Hybridoma Bank	MANDRA-1S
Hoescht 33252	Reagent	Sigma-Aldritch	94403
Phalloidin-AlexaFluor-488	Reagent	Invitrogen/Life Technologies	A12379
Donkey anti-mouse AlexaFluor-647	Reagent	ThermoFisher	A-31571
Zeiss 880 Confocal Microscope	Equipment	Zeiss	
Zen Imaging Software	Software	Zeiss	
Fine Forceps (55)	Equipment	Fine Science Tools	11255-20
p5E:unc503	Plasmid	Addgene	64020
pME:mVenus-CAAX	Plasmid	Addgene	75153
p3E:polyA	Plasmid		
pDest:Tol2-polyA-cryaa:GFP	Plasmid	Addgene	64022
pDest(Tol2)unc503:mVenus-CAAXpA	Plasmid	This study	
Tris Base	Reagent	VWR	97061-794

Tris HCl	Reagent	VWR	97061-258
EDTA,	Reagent	Fisher	BP120-1
LR Clonase-II	Reagent	Ambion	11791100
GeneJET Plasmid Miniprep Kit	Reagent	ThermoFisher Scientific	K0503
mMessage mMachine Kit	Reagent	ThermoFisher Scientific	AM1344
20% Paraformaldehyde	Reagent	Fisher Scientific/Electron Microscopy Sciences	50-980-492
$CaCl_2$ (calcium chloride)	Reagent	Sigma	21115
$MgCl_2$ (magnesium chloride)	Reagent	Sigma-Aldrich	208337
KH_2PO_4 (potassium phosphate)	Reagent	Sigma Aldrich	P9333
Glucose	Reagent	TCI	G0048
NaCl (sodium chloride)	Reagent	Sigma-Aldrich	S9888
KCl (potassium chloride)	Reagent	Sigma Aldrich	P9333
NaHCO3 (sodium bicarbonate)	Reagent	Fisher	BP328-500
Strain, strain background (*Danio rerio*)	Zebrafish Strain	AB line	University of Oregon

Strain, strain background (*D. rerio*)	Zebrafish Strain	urp1^{b1420} line	Bearce et al, 2022 *eLife (10.7554/eLife.83883.)*
Strain, strain background (*D. rerio*)	Zebrafish Strain	urp2^{b1421} line	Bearce et al, 2022 *eLife (10.7554/eLife.83883.)*
Strain, strain background (*D. rerio*)	Zebrafish Strain	uts2r3^{b1436} line	Bearce et al, 2022 *eLife (10.7554/eLife.83883.)*
Leica SP8 Confocal Microscope	Equipment	Leica	